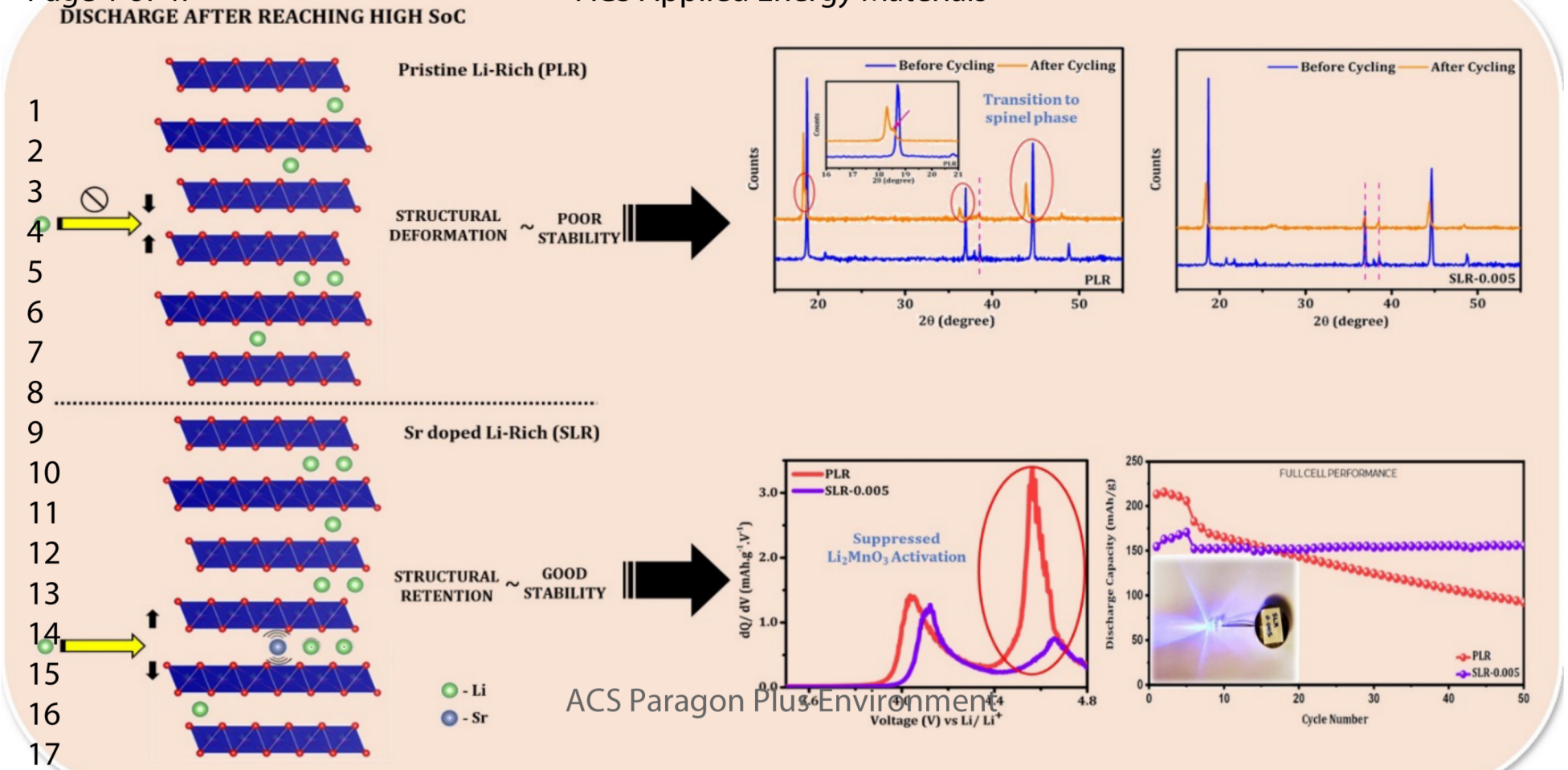

Modulating anion redox activity of $Li_{1.2}Mn_{0.54}Ni_{0.13}Co_{0.13}O_2$ through strong Sr O bond towards achieving stable Li-ion half/ full- cell performance

Vivekanantha Murugan[a,b], Raaju Sundhar Arul Saravanan[a], Kesavan Thangaian[b], Thamodaran Partheeban[b], Vanchiappan Aravindan[c], Madhavi Srinivasan[d], Manickam Sasidharan[b] and Kamala Bharathi Karuppanan[a,e*]

[a]Department of Physics and Nanotechnology, SRM Institute of Science and Technology, Kattankulathur, Chennai, 603 203, Tamil Nadu, India
[b]SRM Research Institute and Department of Chemistry, SRM Institute of Science and Technology, Kattankulathur, Chennai, 603 203, Tamil Nadu, India
[c] Department of Chemistry, Indian Institute of Science Education and Research (IISER), Tirupati, 517507, India.
[d] School of Materials Science and Engineering, Nanyang Technological University, Singapore, 639798.
[e]Nanotechnology Research Center (NRC), SRM Institute of Science and Technology, Kattankulathur, Chennai 603203, Tamil Nadu, India

Corresponding authors: kamalabk@srmist.edu.in

ABSTRACT

Controlled synthesis and compositional modification of Li-rich layered oxides (LLOs) $Li_{1.2}Mn_{0.54}Co_{0.13}Ni_{0.13}O_2$ is considered as a potential strategy to achieve high structural stability/reversibility, suppressed voltage/capacity fading, and realize stable cycle life performance in lithium-ion batteries (LIBs). In this study, the effect of strontium (Sr^{2+}) doping in $Li_{1.2-2x}Sr_xMn_{0.54}Co_{0.13}Ni_{0.13}O_2$ ($0.0015 \leq x \leq 0.007$) is systematically investigated by electrochemical studies. X-ray refinement studies reveal the occupancy of Sr^{2+} at Li^+ (lithium) sites with larger *oxygen-lithium-oxygen* inter-slab spacing in crystal structure. Investigation of Sr^{2+} doped materials in Li-ion cell furnishes up to ~50% reduction in anionic redox activity during the first charge cycle compared to LLO. *Ex-situ* structural analysis of LLO and Sr^{2+}–doped samples shows suppressed layered to spinel phase transformation for the latter. The Sr^{2+}– doped electrode (x=0.005) delivers ~70 Wh kg^{-1} more energy (620 Wh kg^{-1}) than the LLO at 0.2C. Besides, testing for 500 cycles at 1C, Sr^{2+}–doped cathode (x=0.005) retains ~94% of its initial capacity as against LLO (68%). High temperature study at 55 °C shows better electrochemical performance indicating good structural stability of Sr^{2+}–doped samples. Moreover, in full-cell configuration, Sr^{2+}–doped cathode (x=0.005) retains ~98% of its initial capacity at 0.5C after 50 cycles unlike LLO (55%).

KEYWORDS: *Suppressed Anion redox; lithium-rich cathode; Strontium doping; Layered to spinel phase transformation; Full cell performance*

1. INTRODUCTION

In modern society, Li-ion batteries (LIBs) have become an integral part of life, not only powering portable electronic devices but also on the verge of improvising the automobile industry by substituting the conventional fossil fuel[1,2]. Though the LIB technology evolved over half a century ago, insight into basic solid-state chemistry in terms of structure-composition-electrochemical properties is imperative to achieve high energy density, which is a pre-requisite for Electric- and Hybrid Electric Vehicles (EV/HEV)[2,3]. In this perspective, cathode materials play a central role in achieving high working voltage, energy/power densities, life cycles, and cell safety[4,5]. After the introduction of $LiCoO_2$ (α-$NaFeO_2$ structure) as oxide cathode in the late 1990s, numerous studies on engineering cathode structures were made by replacing Na and Fe metals with Li and Co in the layered α-$NaFeO_2$ to achieve high capacities and working voltages [1,6,7]. Though the $LiCoO_2$ (LCO) with a practical capacity of 140 mAh g^{-1} is widely used in portable electronic devices, its primary concern is inadequate energy density (i.e., capacity *x* voltage) owing to limited extraction of Li^+ (~0.5 Li per formula unit) from the crystal structure. Also, the availability of Co-metal is another serious concern. In the past two decades, several efforts were made by the battery community to develop next-generation cathode materials, which opened the door to a new class of $Li(Ni_{1/3}Co_{1/3}Mn_{1/3})O_2$ (NCM-111) cathode after replacing two-third of cobalt metal with Mn and Ni to provide higher specific capacity than native LCO mAh g^{-1}), thermal, and safety features[7,8]. Even though the low-Ni containing NCM-111 delivers better performance over LCO, its performance metrics are insufficient for high power applications and hence, a new class of materials such as Ni–rich $LiNi_{0.8}Co_{0.1}Mn_{0.1}O_2$ (NCM-811), $LiNi_{0.75-x}Co_{0.25}Mn_xO_2$ ($0.1 \leq x \leq 0.25$), $LiNi_{0.8}Co_{0.2}O_2$, and $LiNi_{0.8}Co_{0.15}Al_{0.05}O_2$ (NCA) were progressively developed by minimizing the Co-content, where the Ni content in the transition

metal (TM) was increased gradually to 80 % from 30 % in the base structure NMC−111. These Ni-rich cathodes delivered impressive capacities of up to ~200 mAh g^{-1} at 0.1 C[9-12].

Although the Ni-rich cathodes show a monotonic increase in specific capacity proportional to the Ni-content, rapid capacity fading, and deterioration of cells occur owing to particle's surface degradation, more stable Ni–O formation, and anisotropic volume change vis-à-vis micro cracking. In this context, a new class of Li-rich family cathodes denoted as $Li_{1+x}TM_{1-x}O_2$ or $[x(Li_2MnO_3).1-x(LiTMO_2)]$ (where TM = Mn, Ni, Co, etc.) with a high capacity of >260 mAh g^{-1} received more attention for automotive and high-power applications [8,13-15]. According to Thackeray and Dahn et al., not only some of the Li^+ occupy TM slab in addition to the Li-slab, but also prominent anion redox activity during initial charge occurs, thereby contributing to a high specific capacity. However, the high capacity achieved by this material arises with several challenges such as capacity fading, gradual voltage drop, low initial Columbic efficiency (ICE), and poor rate capability[16-18], which are attributed to a direct consequence of the activation of Li_2MnO_3 phase during the first charge process. The activation of the Li_2MnO_3 component in the first charge cycle ≥ 4.5 V leads to a loss of Li^+ and O from the lattice, which leads to low ICE. In addition, migration of TM ions to Li–slab upon cycling resulting in a structural change to the spinel phase, causing voltage and capacity decay[19-21]. Numerous studies have been performed in the recent past to enhance the electrochemical properties of pristine Li-rich cathodes. For instance, surface coating of Al_2O_3 and Li_2ZrO_3[22-24] was explored to suppress the layered to spinel phase transition as the structural change initially originates at the surface, which subsequently-propagates to the bulk particles. In another strategy, cation doping (Al, Mg, Zr, La, Cr, etc.) was explored to stabilize the bulk lattice structure vis-à-vis increase the Li^+ kinetics, thereby reduce the voltage fading[25-27]. Meanwhile, particle

size reduction was also investigated to enhance the rate capability, which could improve the electronic and ionic conductivity[28,29].

Among other strategies, doping of trace amounts of cations with ionic radii that are similar to or larger than Li^+ has a positive effect over the above-mentioned drawbacks. For instance, Cao et al. partially replaced Li^+ with Na^+, which showed improvement in terms of capacity retention, voltage fade, and also offered high ICE for the doped counterparts[30]. Similarly, Jin et al. doped Al in the Li-layer, which helped to improve the rate capability of the Al-doped cathode with good capacity retention and cycle life[31]. Liang et al. simultaneously doped Na and F to minimize the oxygen loss, thereby enhancing the rate performance and ICE, which showed good capacity retention of ~99 % at 0.2 C[32]. Subsequently, Ramesha et al. doped Ca^{2+} considering the advantages of the stronger Ca–O bond energy, the lower electronegativity of Ca^{2+} compared to Mg^{2+}, and demonstrated that trace amount of Ca^{2+} significantly delayed the layered to spinel transition[33]. Similarly, Manthiram et al. and Aurbach et al. also attempted Mg^{2+} doping, which enhances the structural stability to a larger extent rather than enhancing the discharge capacity[34,35]. In the present study, a systematic attempt was made to enhance the electrochemical properties of $Li_{1.2}Mn_{0.54}Ni_{0.13}Co_{0.13}O_2$ cathode by replacing Li^+ with Sr^{2+}. We chose to investigate Sr as an alternate dopant over other elements because of its stronger Sr–O bond energy compared to other dopants such as Mg and Ca, and lower electronegativity (0.95) compared to Li (0.99) as these properties could significantly impact the rate of anion redox and oxygen loss during the first charge process[26,33-35], thereby expected to suppress the layered to the spinel phase transition. Also, the electrochemical inactive larger Sr^{2+} could act as a pillar without any change in its size and valence upon cycling[35].

2. MATERIALS SYNTHESIS AND CHARACTERIZATION

2.1 Materials and methods

Analytical grade (AR) chemicals such as $MnSO_4$, $(NH_4)_2S_2O_8$, $Ni(NO_3)_2.6H_2O$, $Co(NO_3)_2.6H_2O$, $SrCO_3$, and $LiOH.H_2O$ used for the synthesis were acquired from Sigma-Aldrich with purity > 99.5%. $LiPF_6$ dissolved in the equimolar ratio (1:1) of ethylene carbonate/dimethyl carbonate mixture (EC:DMC 1:1 vol) was obtained from Eager Corporation, Japan. Li-foils and Whatman glass micro-fiber separator was purchased from Sigma-Aldrich. Pristine and Sr-doped Li-rich cathode materials were synthesized by a reactive β-MnO_2 template methodology according to our previous reports[36]. In a typical synthesis of $Li_{1.2}Mn_{0.54}Ni_{0.13}Co_{0.13}O_2$ and $Li_{1.2-2x}Sr_xMn0_{.54}Ni_{0.13}Co_{0.13}O_2$ (x = 0.0015, 0.0030, 0.0050, and 0.0070), stoichiometric amounts of β-MnO_2, $Ni(NO_3)_2.6H_2O$, $Co(NO_3)_2.6H_2O$, $SrCO_3$, and $LiOH.H_2O$ (5% excess) were dispersed in 20 mL of ethanol with constant stirring for 2 h. The resultant mixture was then dried overnight and calcined in air at 900 °C (3 ºC/min) for 15 h to obtain the final products. For subsequent discussion, the as-synthesized samples were labeled as PLR (pristine Li-rich) and SLR-x (x = stoichiometric amount of Sr^{2+}), Sr-doped samples are labeled respectively as SLR-0.0015, SLR-0.003, SLR-0.005, and SLR-0.007.

2.2 Material characterization

The crystal structure and phase purity of the as-synthesized PLR and SLR samples were characterized by X-ray diffraction (Bruker-D8 Advance, Da Vinci) instrument with CuK_α radiation (1.54 Å). Rietveld analysis was conducted using the GSAS program with the EXPGUI graphical interface. The morphological features were probed through a field-emission scanning electron microscope (FE-SEM, Thermo Scientific, Apreo S) and a high-resolution transmission

electron microscope (JEOL JEM-2100) operated at 200 kV. X-ray photoelectron (XPS) spectra were recorded with a Thermo Scientific Spectrometer (model: ESCALAB 250XI) with XR6 micro-focused monochromator (Al-Kα XPS) and XR4 Twin Anode Mg/Al (300/400W) X-ray source. The Al Kα (1486.6 eV) source was operated at 15 kV and 20 mA. Raman spectral measurements were performed using a HORIBA (Japan), LABRAM HR Evolution Micro-Raman spectrometer with an incident laser of wavelength 633 nm.

2.3 Electrochemical characterization

The electrochemical properties of the as-synthesized PLR and SLR samples were evaluated using CR 2032 type coin cells by cyclic voltammetry (CV), galvanostatic cycling with potential limitation (GCPL), and electrochemical impedance spectroscopy (EIS) techniques. Working electrodes for all the studies were prepared by coating a slurry containing 80 wt.% of the active materials (AM), 15 wt.% super-P carbon (SP), and 5 wt.% polyvinylidene difluoride (PVDF) binder using N-methyl pyrrolidone as a solvent, over carbon coated aluminum foil by doctor blade technique. For graphite anode, the slurry containing 90 wt.% graphite, 5 wt.% SP Carbon and 5 wt%. PVDF was coated over copper foil. The coated electrodes were dried at 100 ºC overnight under vacuum conditions and cut into circular disks. The electrodes were stacked in CR-2032 configuration against Li disks separated by a Whatman glass microfiber separator soaked in an electrolyte solution of 1M $LiPF_6$ in EC:DMC (1:1 v/v). The average active mass loading of the electrodes were found to be ~3 mg. Coin cells were assembled in an Ar-filled glove Box (MBraun GmbH, Germany) with oxygen and moisture levels below 0.5 ppm. All the electrochemical measurements were carried out using BCS 805 series battery cycler (Biologic SAS, France). The EIS spectra were measured using VSP 300 Workstation (Biologic SAS, France) in the frequency range of 100 kHz to 10 mHz at 10 mV amplitude. Temperature-

dependent electrochemical analysis was performed using the ESPEC-SH222 tabletop humidity chamber. Full-cells were fabricated using PLR and SLR-0.005 cathode, graphite anode, and were electrochemically tested in the voltage range 1.8 – 4.6 V (*vs*. Li/Li^+)

3. RESULTS AND DISCUSSION

3.1 Synthesis, structural, and electrochemical properties of as-synthesized Sr-doped SLR

The pristine Li-rich $Li_{1.2}Mn_{0.54}Co_{0.13}Ni_{0.13}O_2$ (**PLR**) and Sr-doped $Li_{1.2-2x}Sr_xMn_{0.54}Co_{0.13}Ni_{0.13}O_2$ ($0.0015 \leq x \leq 0.007$, **SLR**) materials were synthesized using β–MnO_2 nanorods as a reactive template as well as Mn source following our previous report[36]. The SLR-0.0015, SLR-0.003, SLR-0.005, SLR-0.007, and PLR materials readily form upon mixing of the β-MnO_2 template with a stoichiometric ratio of $Ni(NO_3)_2.6H_2O$, $Co(NO_3)_2.6H_2O$, $SrCO_3$, and $LiOH.H_2O$ (5% excess) followed by high-temperature sintering as shown in **Scheme 1**. The formation of *O3* type layered PLR and SLR materials with *R3–m* space group (α–$NaFeO_2$ structures) is very obvious from the XRD reflections presented in **Fig. 1,** albeit with few additional weak reflections from 20 to 25° which is ascribed to the characteristic Li_2MnO_3 component (space group *C2/m*) as well as the existence of short-range ordered Li-ions in the transition metal layer[14,37]. It is apparent from the XRD patterns that Sr-doping in PLR did not affect the formation of Li-rich compound where the presence of both layered and monoclinic phases is quite obvious. The cation ordering between Li-slab and TM-slab largely controls the rate capability and voltage decay. Thus the degree of cation mixing estimated from the intensity ratio of high intense (I_{003}/I_{104}) reflections for PLR, SLR-0.0015, SLR-0.003, SLR-0.005, and SLR-0.007 was found to be 1.59, 1.94, 1.88, 1.90, and 1.79, respectively, which is larger than the standard 1.2 level confirming a lower degree of cation mixing in the Li-layer[37]. Thus, replacing a small amount of

monovalent Li^+ with larger divalent Sr^{2+} reduces the Li/Ni cation intermixing by minimizing the occupancy of $Ni^{2+/3+}$ ions in the Li-layer and vice versa. A typical crystalline layered structure of the SLR series is also established from the clear peak splitting between the (*006*)/(*102*) and (*018*) / (*110*) reflections revealing a high degree of hexagonal ordering[38].

Preliminary CV traces of PLR and SLR cathodes in the potential window 2.0–4.8 V recorded at the scan rate of 0.2 mV s^{-1} is displayed in **Fig. 2a-e**. As seen from **Fig.2,** the first cycle redox behavior of both PLR and SLR cathodes are quite different from remaining cycles indicating a characteristic "activation" of the Li_2MnO_3 phase to give electrochemically active Li_xMnO_2 ($Mn^{3+/4+}$redox) with concomitant oxygen removal in the form of Li_2O from the lattice above 4.5 V. The high intense anodic peak at ~3.9 V is ascribed to oxidation of Ni and Co, a typical characteristic of Li-rich materials. Upon the reverse cathodic scan, the peaks at ~3.7 V and ~3.3 V correspond to Ni/Co and Mn^{4+}, respectively[39]. Comparison of 1st cycle anodic scans of PLR and SLR cathodes reveals that the peak intensity of Li_2MnO_3 activation gradually reduces with increasing Sr content. It is likely that higher Sr–O bond energy (425.5 ±16.7 kJ.mol^{-1}) compared to the Li–O bond (333.5 ±8.4 kJ.mol^{-1}) coupled with a lower electronegativity value of Sr (0.95) could suppress the oxygen loss and anion redox activity of SLR cathodes. Besides, the comparison plot of CV traces (upto 5 cycles) of SLR series reveals (**Fig. 2f**) that SLR-0.005 cathode furnished minimal structural transformation to spinel phase (anodic peak ~3.3 V) and employed for subsequent electrochemical investigations.

Initial (dis)charge was performed by GCPL technique at 0.5 C (1 C = ~250 mA g^{-1}) in the voltage window of 2.0–4.8 V (*vs.* Li/Li^+) and **Fig. 3a** compares the 1st cycle plots of both PLR and SLR cathodes. All the first cycle charge profiles show a voltage ramp from 3.9–4.4 V and a signature plateau at 4.4–4.6 V where the former is related to Li^+ (de)intercalation from the

layered structure, while the latter is ascribed to activation of Li_2MnO_3 with associated anionic reactions forming O_2 and/or peroxo-like $(O_2)^{n-}$ species. The length of the plateau region at ~4.5 V during the first charge is very critical as it influences the reversible capacity, and it is very obvious from **Fig.3a** that the length of the plateau gradually shortens upon increasing Sr-dopant content from SLR-0.0015 to SLR-0.007. The first charge and discharge capacities for PLR, SLR-0.0015, SLR-0.003, SLR-0.005, and SLR-0.007 were 296/217, 257/185, 235/ 164, 200/150, and 222/157 mAh g^{-1}, respectively with corresponding Coulombic efficiencies of 73, 71.9, 72.3, 75.0, and 70.7 %. Additionally, the capacity contribution due to cation (de)intercalation up to 4.5 V, anionic redox couple at 4.5–4.6 V, and oxygen loss at 4.6–4.8 V were estimated according to Bruce et al.[40]. The capacity estimated from Ni/Co oxidation was found to be 130, 123, 120, 123, and 114 mAh g^{-1} for PLR, SLR-0.0015, SLR-0.003, SLR-0.005, and SLR-0.007, respectively; whereas the capacity contribution from anionic redox species $(O_2)^{n-}$ at the 4.5 V plateau were 80, 56, 49, 27, and 36 mAh g^{-1} for PLR, SLR-0.0015, SLR-0.003, SLR-0.005 and SLR-0.007, respectively. Similarly, the capacity originated from the loss of lattice O_2 was 86, 78, 67, 50, and 72 mAh g^{-1} for PLR, SLR-0.0015, SLR-0.003, SLR-0.005, and SLR-0.007, respectively. The above results indicate that the capacity contribution from anionic redox species and lattice oxygen release at $\geq$ 4.5 V has been appreciably reduced rather than TM redox process. The above observation is also evident from discharge cycles where suppressed anionic reduction activity and O_2 loss at $\leq$ 3.7 V were noted, unlike Ni/Co reduction profiles. The optimized SLR-0.005 electrode delivered a discharge capacity of 187 mAh g^{-1} and discharge energy density values of 620 Wh kg^{-1} compared to PLR (170 mAh g^{-1} with the energy of 551 Wh kg^{-1}) after 125 charge-discharge cycles at 0.5 C rate (**Fig. 3b, Fig. S1d).** The comparative GCPL plots for PLR and SLR-0.005 are given in **Fig. 3c-d**, and for the other Sr^{2+}

materials in **Fig. S1a-c**. It is observed that PLR displayed rapid capacity and voltage decay upon cycling, and among the Sr^{2+} doped samples, SLR-0.005 showed the least capacity/ voltage decay. From the average discharge voltage plot (**Fig. 3e)**, the estimated voltage drop after 125 cycles for PLR, SLR-0.0015, SLR-0.003, SLR-0.005, and SLR-0.007 were 0.360, 0.337, 0.366, 0.330 and 0.356 V, respectively, with SLR-0.005 delivering ~ 0.15 V higher average voltage than PLR. Among the various samples, SLR-0.005 delivered the best results, and on further increasing the dopant concentration (SLR-0.007), the electrochemical properties rather deteriorated, maybe due to the partial hindrance of Li-ion diffusion by Sr^{2+} at high concentration and fractional Sr^{2+} occupancy in TM layer[33,34]. This was confirmed by measuring the Li-ion diffusion co-efficient for all the samples after cycling using the following equation[31],

$$D = \frac{R^2T^2}{2A^2n^4F^4C^2\sigma^2}$$

where R is the gas constant, T is the absolute temperature, A is the area of the electrode, n is number of electron transfer per molecule, F is the Faraday's constant and C is the concentration of Li^+ per unit cell, σ is the Warburg factor obtained from linear fitting of the low frequency region from the EIS plot **(Fig. S2)**, and $\boldsymbol{\omega} = 2\pi f$. All samples showed Nyquist patterns consisting of (i) high-frequency region (related to solution resistance, R_s), (ii) mid-frequency region (related to charge transfer resistance, R_{ct}), and (iii) low-frequency Warburg feature (related to Li-ion diffusion in electrode materials)[33] . The resistance values for all the samples are given in **Table S7**. The calculated Li^+ diffusion values for PLR, SLR-0.0015, SLR-0.003, SLR-0.005 and SLR-0.007 are 5.901, 5.282, 5.088, 4.407, 5.463 x 10^{-15} cm^2 s^{-1}. The improved Li-ion diffusion kinetics for Sr doped samples can be attributed to the lower Li/Ni intermixing, increased O-Li-O interslab distance caused by larger Sr^{2+} ions and suppressed TM ion migration[41]. **Fig.3f**

compares the rate capability of PLR with SLR-0.005 at different current densities of 0.2, 0.5, 1.0, 2.0, and 5.0 C, where the PLR indeed delivers marginally higher discharge capacities overdoped SLR samples, but the capacity difference between them gradually decreases as the current rate increases. Thus, upon increasing current densities, the difference in capacities between PLR and SLR-0.005 gradually narrows down from ~70 mAh g^{-1} at 0.2 C to ~12 mAh g^{-1} at 5 C indicating a good rate capability of the latter. The good capacity retention characteristic of SLR-0.005 over PLR at a higher C rate is reasoned to the expansion of *c* lattice upon larger Sr^{2+} doping in the Li-slab that helps in facile Li^{+} (de)insertion[31,33,41].Though the capacity of the SLR sample is lower than the PLR counterpart, but the former displayed better capacity retention at higher C rates.

Further, one can also argue that the difference in electrochemical performance could also originate from particle size and morphology since surface texture could play a critical role over electrochemical properties. Morphological investigation of PLR and SLR samples with FE-SEM and HR-TEM (**Fig.S3b-f**) confirms the retention of 1D rod morphology of β-MnO_2 **(Fig.S3a)** with an aspect ratio of ~1000 nm length and width ~450 nm. In addition, the HR-TEM image (**Fig.S3f)** showed lattice fringes with a spacing of ~0.46 nm, which is in good agreement with the (*003*) plane of rhombohedral structure or the (*001*) reflection of the monoclinic structure[42]. Similar to PLR, Sr-doped SLR-0.005 shows retention of 1D structure with a comparable aspect ratio (**Fig. 4a-c**) where the elemental mapping (**Fig. 4d-i)** also clearly confirms the presence of Sr in the layered lattices. Furthermore, high-resolution TEM images and electron diffraction pattern (SAED, **Fig. 4j-m**) proves high crystallinity that can be indexed to the hexagonal structure with *R-3m* and *C2/m* phases corroborating well with the XRD data. Accordingly, as PLR and SLR-0.005 have similar particle size and morphology, the observed electrochemical properties can be related to Sr-doping, where the role of particle size and morphology can be

ruled out. Undoubtedly, the Sr-doping suppressed the anionic redox activity and O_2 release from the lattices at ≥ 4.4 V, and to make this point clear, we further performed several experiments to understand the performance of Sr-doped Li-rich cathodes.

3.2 Effect of Sr-incorporation on the crystal structure

XRD Rietveld refinement based on both trigonal (*R3-m*) and monoclinic (*C2/m*) phases of PLR and SLR-0.005 samples have been performed to study the influence of Sr-doping (**Fig. 5a-b)**. Refinement of SLR-0.005 with Sr^{2+} occupancy at various sites (2c, 2b, 4h, 4g) were done and the refinement parameters are given in Table S2-S5, supporting information. Analysis of refinement data suggests the preferential occupation of Sr^{2+} at Li^+ *2c* sites **(Tables S6,** supporting information**)** from the weighted *R*-factor R_{wp} of SLR-0.005 (5.7%), which is lower than the PLR (R_{wp} ~7.8%) **(Table 1)**. It is observed that doping of a small amount of Sr^{2+} (0.5 wt%) results in a slight increase in lattice parameter *c* (**Table 1**) similar to Na^+-doped Li-rich oxides[43]. However, the occupancy of larger Sr^{2+} (1.13 Å) in an ideal 6-coordination would result in slight lattice distortion and strain, resulting in a slight decrease in the *b* lattice parameter. Moreover, the argument of Sr^{2+} ion residing in the diffusion channel of Li-slabs would result in hindrance to diffusion of Li^+ vis-à-vis rate performance; however, one has to note that such a blockage of Li^+ is insignificant at such a low level of dopant concentrations (0.005 moles). Additionally, O-Li-O inter-slab spacing (I_{LiO_2}) is considered to be critical for the Li^+ ion diffusion during cycling was calculated using the equation

$$I_{LiO_2} = \frac{C_{hex}}{3} - \left(\frac{2}{3} - 2Z_{ox}\right)C_{hex}$$

where, C_{hex} is the lattice constant *c,* and Z_{ox} represents the *6c* site oxygen position along the c-axis and assigns a value of 0.244[44]. The calculated inter-slab distance for PLR and SLR-0.005 are

2.1199 and 2.1260 Å, respectively. The increased I_{LiO_2}value of SLR-0.005 could explain the enhancement of its electrochemical performance. Furthermore, the *ex-situ* XRD analysis of PLR and SLR-0.005 after first charge and discharge is compared with the fresh electrode **(Fig. 5c-d)**. After charging to 4.8 V a shoulder peak at ~ 18.6 ° belonging to the spinel like structure was observed for PLR **(Fig. 5c),** due to the migration of Li and TM ions to nearby tetrahedral sites[44]. Also, the inset graphs in **Fig. 5c-d** shows the absence of layered reflections for PLR after charging, these observations suggest that SLR-0.005 retains the layered structure to a greater extend than PLR. After discharging, both PLR and SLR-0.005 show similar patterns to fresh electrode, except for the Li_2MnO_3 peaks, confirming its structural reversability. Ex-situ XRD patterns after cycling at 0.5 C for 125 cycles was performed and compared with the patterns before cycling **(Fig. 5e-f)**. After charge/discharge cycling, the PLR electrode **(Fig. 5e)** showed the presence of a new spinel phase after dsicharge, as evident from the shoulder peak observed at ~ 18.6° and additional peaks at ~ 36° and 43°[45,46]. No such reflections were observed in SLR-0.005 after cycling **(Fig. 5f)**, thereby confirming the suppression of layered to the spinel phase transition for SLR-0.005. Besides, a minor shift in XRD reflections toward lower angles for both PLR and SLR-0.005 is attributed to the lattice distortions.

To get more insight into the local environment, XPS spectra of PLR and SLR-0.005 samples were recorded to examine the oxidation states of different elements. The pristine sample showed core level photoelectron peaks of all elements; for instance, Mn *2p* (**Fig. S4a)** consists of two major spin-orbit split peaks, which were further de-convoluted at 642.7 ($2p_{3/2}$) and 654.8 eV ($2p_{1/2}$) that are assigned to Mn^{4+}, and peaks at 641.3 and 653.0 eV corresponding to Mn^{3+} oxidation states[47,48]. The Co *2p* spectrum (**Fig. S4b)** similarly consists of two spin split orbits which were de-convoluted to peaks ~780.3 ($2p_{3/2}$) and 795.6 eV ($2p_{1/2}$) belonging to Co^{3+}, along

with peaks at 778.9 and 794.20 eV ascribed to Co^{2+}[49,50]. Likewise, Ni *2p* (**Fig. S4c)** signal consists of two major peaks at 854.1 ($2p_{3/2}$), and 871.7 eV ($2p_{1/2}$), which are assigned to Ni^{2+} and the presence of peaks at 855.8 and 874.5 eV is related to Ni^{3+} [51]. The corresponding shakes off satellites are also observed adjacent to the major peaks due to sudden change in Coulombic potential of ejected electrons when passes through the valence band. The *O 1s* spectrum (**Fig. S4d)** was de-convoluted into three peaks corresponding to O^{2-}, OH^- / adsorbed oxygen at 528.4, 529.8, and 531.6 eV, respectively[37,52]. The XPS spectra for SLR-0.005 are shown in **Fig. 6a-f**. Similar to PLR, Mn *2p* (**Fig. 6a)** consists of deconvoluted peaks at 642.5 ($2p_{3/2}$) and 654.3 eV ($2p_{1/2}$) assigned to Mn^{4+}, and signals at 640.8 and 652.5 eV corresponding to Mn^{3+} oxidation states. Similarly, Co *2p* spectrum (**Fig. 6b)** was de-convoluted into 780 ($2p_{3/2}$) and 795.2 eV ($2p_{1/2}$) belonging to Co^{3+}, along with peaks at 778.7 and 793.90 eV corresponding to Co^{2+}. The Ni *2p* (**Fig. 6c)** spectrum showed two major peaks at 853.5 ($2p_{3/2}$) and 871 eV ($2p_{1/2}$), which are assigned to Ni^{2+}, while the binding energies 855.2 eV and 873.9 eV are assigned to Ni^{3+}. More importantly, Sr *3d* (**Fig. 6d)** spectrum presents two deconvoluted peaks ~132.6 (Sr $3d_{5/2}$) and ~134.2 eV (Sr $3d_{3/2}$) indicating the presence of Sr[53]. The O *1s* spectrum (**Fig. 6e)** was de-convoluted into three peaks corresponding to O^{2-}, OH^- /adsorbed O_2 at 527, 529.4, and 531 eV, respectively. More interestingly, in comparison of XPS spectra of different elements for PLR and SLR-0.005 (**Fig. 6f-j)**, a shift towards the lower binding energy was observed for the latter. It is reasoned out that Li has higher electronegativity compared to Sr resulting in an increased electron density around the elements causing a shift to lower binding energies,[54] thereby confirming the successful doping of Sr in the crystal lattice. Additionally, Raman spectra obtained for PLR and SLR-0.005 (**Fig. S5 a-b)** showed typical Li-rich features with A_{1g} and E_g stretching modes corresponding to the layered *R3–m* structure along with the presence B_g peak

confirming the Li_2MnO_3 phase[55]. Apparently, the appearance of an additional shoulder peak above 650 cm^{-1} for PLR **(Fig S5a)** ascribed to the spinel phase corroborating *ex-situ* XRD data. However, for SLR-0.005, a significant peak was not observed above 650 cm^{-1} but there was a slight broadening of A_{1g} peak, revealing the formation of spinel phase in the samples after 125 cycles at 0.5 C.[45]

3.3 Influence of Sr-doping over the electrochemical properties

Li-rich layered oxides (LLO) often have inferior cycling stability, voltage decay, and structural stability. To get more understandings on materials electrochemical and structural correlation, the dQ/dV plots were plotted for PLR and SLR-0.005 (**Fig. 7**). The first cycle dQ/dV plot of SLR-0.005 (**Fig. 7a)** clearly endorses repressed Li_2MnO_3 activation over the PLR counterpart. Nonetheless, the cathodic peak of pristine PLR compared to SLR-0.005 is shifted to below 3.0 V after 125 cycles (**Fig. 7b)** owing to layered-spinel transformation, induced by lattice oxygen removal and subsequent TM ion migration into Li-slab, with subsequent formation of an additional peak just above 2.5 V owing to $Mn^{3+/4+}$ redox couple in the spinel phase. On charging, the $Mn^{3+/4+}$ redox couple of secondary spinel phase appears just >3.0 V. Apparently, Sr^{2+}doping thus controls the capacity and voltage fading by acting as a stabilizing pillar between the Li layers as well as prevents cation mixing upon cycling[34]. The appearance of an oxidation peak at >4.5 V for SLR-0.005 until the 4^{th} cycles (associated with Li_2MnO_3 oxidation), while the absence of a similar feature for PLR **(Fig. 7c-d)** indeed demonstrates sluggish Li_2MnO_3 activation upon Sr^{2+} doping. The presence of redox peaks between 3.0–3.5 V is directly associated with Li_2MnO_3 activation **(Fig 7c-d)**. The typical cathodic peak at ~3.2 V is related with $Mn^{3+/4+}$ couple along with anion redox (e.g., O_2^{2-}/O_2^{-}) where both the samples show a gradual increase in the peak intensity albeit with the lower current for SLR-0.005 **(Fig. 7d)**

compared to PLR sample. Likewise, on the anodic scan, there is a significant difference in the peak features between 3.2 V and 3.5 V for PLR and SLR-0.005 due to $Mn^{3+/4+}$ couples, where the former exhibit high intense peaks[56]. In addition, the PLR sample shows a much prominent oxidation peak at ~4.2 V associated with anion oxidation, indicating pronounced anionic redox activity **(Fig. 7c)**. It is worthwhile to note that SLR-0.005 show lower shift in voltage and suppressed spinel $Mn^{3+/4+}$ redox current compared to PLR proving that Sr-doping controls the anionic redox properties and O_2 release vis-à-vis structural and electrochemical stability.

Investigation of long cycle stability test of PLR and SLR-0.005 was conducted for 500 cycles at 1 C rate (**Fig. 8a**) and displayed an initial discharge capacity of 175 and 124 mAh g^{-1}, respectively. Upon continuous cycling, the observed capacity difference between PLR and SLR-0.005 gradually narrows down, and SLR-0.005 attained a stabilized capacity of ~ 150 mAh g^{-1} at around 150 cycles. After 500 cycles, the SLR-0.005 electrode delivers ~140 mAh g^{-1} against ~115 mAh g^{-1} for PLR. It is worthy of mentioning that the SLR-0.005 electrode retained ~94 % of its capacity after stabilizing, with ≥ 99% Coulombic efficiency (excluding the first cycle) as against 65 % retention of PLR. Additionally, the plot of energy density *vs.* cycle number (**Fig. 8b**) clearly shows that the SLR-0.005 electrode delivers ~100 Wh kg^{-1} higher energy density owing to high capacity retention and lower voltage decay compared to the PLR counterpart. One significant difference observed for SLR-0.005 at 0.5 C and at 1 C is the low initial capacity and its gradual increase upon cycling. Supressed Li_2MnO_3 activation results in the low initial capacity. The increase in capacity can be attributed to two factors, (i) the activation of Li_2MnO_3 in the subsequent cycles as seen in **Fig 7d**, and (ii) at higher rates, firstly, the surface of the electrode is accessed by the electrolyte and activated, followed by the activation of interior regions upon cycling resulting in the gradual increase in capacity, this effect is more pronounced

at 1C and hence it takes more cycles for the electrode to reach its maximum capacity. SLR–0.005 retained nearly 83 % of initial voltage (**Fig. 8c)** as against 77% of PLR with lower voltage decay. It is also clearly evident from average voltage *vs.* cycle number plots (**Fig. 8d-e**) that the existence of voltage hysteresis or voltage fading for both pristine and SLR-0.005 samples, where the difference between charge and discharge voltages after 500 cycles was 1.49 V for PLR (**Fig. 8d)** compared to 1.24 V for SLR-0.005 (**Fig. 8e)**. Furthermore, the voltage fading between the initial and final cycle for SLR-0.005 was found to be merely 57 mV as against 120 mV of PLR, perhaps due to a large impedance buildup of PLR upon cycling[34]. It is observed from EIS graphs (**Fig. S6a-b**) that SLR-0.005 shows slightly higher R_{ct} compared to PLR during initial cycles; however, SLR-0.005 exhibited a very low R_{ct} and R_s over PLR **(Table S8)**, corroborating the voltage hysteresis data as discussed in **Fig. 8d-e**. Additionally, the calculated Li^+ ion diffusion coefficient (D) from curve fitted EIS data **(Fig. S6a inset)** was found to be 1.294×10^{-13} cm^2 s^{-1} for SLR-0.005 which is higher than PLR electrode (2.806×10^{-14} cm^2 s^{-1}). Moreover, it is also evident that Sr-doping hampers the layered to spinel transition of SLR-0.005 even after 200 cycles compared to PLR, as evident from dQ/dV plots (**Fig. S7**). The comparative dQ/dV profiles for every 100th cycle for SLR-0.005 are shown in **Fig. S7c-f**. The cathodic peak is centered around 2.75 V with no significant voltage change after the 100th cycle, whereas the cathodic peak gradually shifts towards lower voltage for PLR and reached ~ 2.45 V after 500 cycles indicating layered to spinel transformation.

To investigate the electrochemical performance of Sr-doped SLR-0.005, the cycling was performed at 1 C rate for 110 cycles at an elevated temperature of 55 °C, as shown in **Fig.9**. The observed discharge capacity, energy density, and average voltage (**Fig. 9a-c)** are similar to that of data acquired at ambient temperature. The SLR-0.005 retained 75 % capacity equivalent to

575 Wh.kg^{-1} energy density after 110 cycles as against only 64% (~70 Wh kg^{-1}) of PLR. Interestingly, unlike room temperature behavior, the plot of initial dQ/dV curves for PLR and SLR-0.005 (**Fig. 9d)** revealed that the Li_2MnO_3 activation peak intensity substantially increases for the latter with concomitant high capacity at >4.5 V similar to PLR in agreement with the previous report[36]. The dQ/dV plots at regular intervals of cycling (**Fig. 9e-f**) exhibit a high intense reduction peak for SLR-0.005 ~0.25 V higher than the PLR, confirming the positive effect of Sr-doping even at increased Li_2MnO_3 activation level. Such positive effects of Sr-doping are also seen on the anodic scan, where the $Mn^{3+/4+}$and anion redox activity decreases for SLR-0.005 at high-temperature conditions, corroborating the above results.

Furthermore, we have also investigated the performance of full-cells for PLR and SLR-0.005 to ensure the compatibility by pairing with graphite, as shown in **Fig. 10** in ambient temperature conditions. Graphite half cell data is given in **Fig. S8**. The anode to cathode ratio for PLR was 1.2: 1 and for SLR-0.005 was 1.5: 1. The cells were cycled initially at 0.1 C (1C = 250 mAh.g^{-1}) for 5 cycles and subsequently cycled at 0.5 C in the voltage window 1.8–4.6 V. The first cycle charge/discharge capacities were 300/213 and 256/154 mAh g^{-1} for PLR and SLR-0.005, respectively (The capacity values are calculated with respect to cathode mass) (**Fig. 10a)**. Similar to half-cell studies, the capacity contribution from the anionic redox couples and O loss is again higher for PLR in the full-cell configuration. The discharge capacity *vs.* cycle number plot shows that the SLR-0.005 electrode delivered ~155 mAh g^{-1} after 50 cycles compared to 95 mAh g^{-1} for PLR (**Fig. 10b)**. Furthermore, the SLR-0.005 cathode retained 90 % of its initial capacity (**Fig. 10b inset)** after 100 cycles**. Fig. 10c-d** gives the GCPL plots of PLR and SLR-0.005 at different cycles, which clearly indicates suppressed voltage and capacity fading of SLR

–0.005. Full cell fabricated using SLR –0.005 was used to light a blue LED as shown in **Fig. 10d(inset).**

3. CONCLUSION

We have successfully demonstrated the synthesis of $Li_{1.2-x}Sr_xMn_{0.54}Ni_{0.13}Co_{0.13}O_2$ by a simple reactive template methodology to reduce voltage decay and improve the rate capability of pristine LLOs. XRD Rietveld refinement, Raman spectral analysis, *ex-situ* analysis of cycled cells, and XPS analysis established the successful doping of Sr^{2+} ions in the Li-layer. Electron microscopes observation of both PLR and SLR-0.005 revealed rod-like morphology inferring insignificant change in surface properties. Thorough electrochemical investigation of Sr-doped SLR samples demonstrated a repressed Li_2MnO_3 activation vis-à-vis reduced anionic activity as well as O_2 loss. With increased Sr-doping content, the capacity contribution at ≥ 4.5 V from anionic redox and O_2 loss significantly reduced. The Sr-doped samples outperformed the pristine sample in terms of capacity and voltage retention, with SLR-0.005 retaining almost 94 % of its maximum capacity after 500 cycles at 1 C. Contrary to suppressed Li_2MnO_3 activation at ambient temperature, testing of Sr-doped cathode at 50 °C demonstrated complete Li_2MnO_3 activation during the first charge itself. Analysis of voltage hysteresis revealed merely 0.52 V decay for SLR-0.005 over PLR after 500 cycles with 100 Wh kg^{-1} more energy density. Investigation of SLR-0.005 in full-cell configuration with graphite retained ~98 % of its initial capacity at 0.5 C compared to 55 % retention for PLR counterpart. Therefore, reduced anionic activity, low O_2 liberation, minimal voltage decay/capacity fading, and the pillaring effect of Sr-doping are strongly expected to be beneficial for the improvement of LLOs.

ASSOCIATED CONTENT

Supplementary Information

Rietveld refinement parameters for PLR and SLR-0.005 with Sr^{2+} integration at various site, resistance and Li-ion diffusion values for all samples at 0.5 C, resistance and Li-ion diffusion values for PLR and SLR-0.005 at 1 C, comparative dQ/ dV and energy density plots of all samples at 0.5 C, EIS spectra for all samples at 0.5 C, FE-SEM and TEM images of of PLR, XPS spectra of PLR, Rmana spectra of PLR and SLR-0.005, EIS spectra of PLR and SLR-0.005 at 1 C, comparative dQ/ dV plots of PLR and SLR-0.005 at 1C, half-cell data for graphite anode.

AUTHOR INFORMATION

* To whom all correspondence should be addressed,

E-mail: kamalabk@srmist.edu.in

ORCID ID

Kamala Bharathi Karupannan: 0000-0002-8466-9400

Manickam Sasidharan: 0000-0002-0795-7062

Srinivasan Madhavi: 0000-0002-5497-3428

Vanchiappan Aravindan: 0000-0003-1357-7717

Kesavan Thangian: 0000-0003-1030-4270

Murugan Vivekanantha: 0000-0002-3531-2915

Notes

The authors declare there is no conflict of interest.

ACKNOWLEDGMENT

M. S. thanks MNRE (Ministry of New and Renewable Energy, No.31/03/2014-15/PVSE-R&D), for financial assistance. This work was also partially funded by the National Research Foundation of Singapore, Investigatorship Award Number NRFI2017-08 and Singapore-HUJ Alliance for Research and Enterprise (SHARE), Nanomaterials for Energy and Energy-Water Nexus (NEW), grants from the National Research Foundation, Prime Minister's Office, Singapore under its Campus of Research Excellence and Technological Enterprise (CREATE). V.A. acknowledges the financial support from the Department of Science & Technology, Govt. of India through Swarnajayanti Fellowship (DST/SJF/PSA-02/2019-20). M. V. thanks SRM SCIF for XRD, Micro Raman, FE-SEM, and HR-TEM facilities. M. V. thanks CSIR for providing Senior Research Fellowship.

REFERENCES

(1) Zhan, C.; Wu, T.; Lu, J.; Amine, K. Dissolution, Migration, and Deposition of Transition Metal Ions in Li-Ion Batteries Exemplified by Mn-Based Cathodes-A Critical Review. *Energy Environ. Sci.* **2018**, *11* (2), 243–257. https://doi.org/10.1039/c7ee03122j.

(2) Wang, X.; Ding, Y. L.; Deng, Y. P.; Chen, Z. Ni-Rich/Co-Poor Layered Cathode for Automotive Li-Ion Batteries: Promises and Challenges. *Adv. Energy Mater.* **2020**, *10* (12), 1–28. https://doi.org/10.1002/aenm.201903864.

(3) Yoon, C. S.; Park, K. J.; Kim, U. H.; Kang, K. H.; Ryu, H. H.; Sun, Y. K. High-Energy Ni-Rich $Li[Ni_xCo_yMn_{1-x-y}]O_2$ Cathodes via Compositional Partitioning for Next-Generation Electric Vehicles. *Chem. Mater.* **2017**, *29* (24), 10436–10445. https://doi.org/10.1021/acs.chemmater.7b04047.

(4) Choi, J. W.; Aurbach, D. Promise and Reality of Post-Lithium-Ion Batteries with High Energy Densities. *Nat. Rev. Mater.* **2016**, *1*. https://doi.org/10.1038/natrevmats.2016.13.

(5) Nitta, N.; Wu, F.; Lee, J. T.; Yushin, G. Li-Ion Battery Materials: Present and Future. *Mater. Today* **2015**, *18* (5), 252–264. https://doi.org/10.1016/j.mattod.2014.10.040.

(6) Wang, J.; He, X.; Paillard, E.; Laszczynski, N.; Li, J.; Passerini, S. Lithium- and Manganese-Rich Oxide Cathode Materials for High-Energy Lithium Ion Batteries. *Adv. Energy Mater.* **2016**, *6* (21). https://doi.org/10.1002/aenm.201600906.

(7) Etacheri, V.; Marom, R.; Elazari, R.; Salitra, G.; Aurbach, D. Challenges in the Development of Advanced Li-Ion Batteries: A Review. *Energy Environ. Sci.* **2011**, *4* (9), 3243–3262. https://doi.org/10.1039/c1ee01598b.

(8) Rozier, P.; Tarascon, J. M. Review—Li-Rich Layered Oxide Cathodes for Next-Generation Li-Ion Batteries: Chances and Challenges. *J. Electrochem. Soc.* **2015**, *162* (14), A2490–A2499. https://doi.org/10.1149/2.0111514jes.

(9) Liao, P. Y.; Duh, J. G.; Sheen, S. R. Effect of Mn Content on the Microstructure and Electrochemical Performance of LiNi[Sub 0.75−x]Co[Sub 0.25]Mn[Sub x]O[Sub 2] Cathode Materials. *J. Electrochem. Soc.* **2005**, *152* (9), A1695. https://doi.org/10.1149/1.1952687.

(10) Kim, M. H.; Shin, H. S.; Shin, D.; Sun, Y. K. Synthesis and Electrochemical Properties of $Li[Ni_{0.8}Co_{0.1}Mn_{0.1}]O_2$ and $Li[Ni_{0.8}Co_{0.2}]O_2$ via Co-Precipitation. *J. Power Sources* **2006**, *159* (2), 1328–1333. https://doi.org/10.1016/j.jpowsour.2005.11.083.

(11) Chen, C. H.; Liu, J.; Stoll, M. E.; Henriksen, G.; Vissers, D. R.; Amine, K. Aluminum-Doped Lithium Nickel Cobalt Oxide Electrodes for High-Power Lithium-Ion Batteries. *J. Power Sources* **2004**, *128* (2), 278–285. https://doi.org/10.1016/j.jpowsour.2003.10.009.

(12) Liu, W.; Oh, P.; Liu, X.; Lee, M. J.; Cho, W.; Chae, S.; Kim, Y.; Cho, J. Nickel-Rich Layered Lithium Transition-Metal Oxide for High-Energy Lithium-Ion Batteries. *Angew. Chemie - Int. Ed.* **2015**, *54* (15), 4440–4457. https://doi.org/10.1002/anie.201409262.

(13) Nayak, P. K.; Erickson, E. M.; Schipper, F.; Penki, T. R.; Munichandraiah, N.; Adelhelm, P.; Sclar, H.; Amalraj, F.; Markovsky, B.; Aurbach, D. Review on Challenges and Recent Advances in the Electrochemical Performance of High Capacity Li- and Mn-Rich Cathode Materials for Li-Ion Batteries. *Adv. Energy Mater.* **2018**, *8* (8), 1–16. https://doi.org/10.1002/aenm.201702397.

(14) Thackeray, M. M.; Kang, S. H.; Johnson, C. S.; Vaughey, J. T.; Benedek, R.; Hackney, S.

A. Li_2MnO_3-Stabilized $LiMO_2$ (M = Mn, Ni, Co) Electrodes for Lithium-Ion Batteries. *J. Mater. Chem.* **2007**, *17* (30), 3112–3125. https://doi.org/10.1039/b702425h.

(15) Lu, Z.; Beaulieu, L. Y.; Donaberger, R. A.; Thomas, C. L.; Dahn, J. R. Synthesis, Structure, and Electrochemical Behavior of Li[Ni[Sub x]Li[Sub 1/3−2x/3]Mn[Sub 2/3−x/3]]O[Sub 2]. *J. Electrochem. Soc.* **2002**, *149* (6), A778. https://doi.org/10.1149/1.1471541.

(16) Wang, Y.; Wang, L.; Guo, X.; Wu, T.; Yang, Y.; Wang, B.; Wang, E.; Yu, H. Thermal Stability Enhancement through Structure Modification on the Microsized Crystalline Grain Surface of Lithium-Rich Layered Oxides. *ACS Appl. Mater. Interfaces* **2020**, *12* (7), 8306–8315. https://doi.org/10.1021/acsami.9b21303.

(17) Zhao, J.; Huang, R.; Ramos, P.; Yue, Y.; Wu, Q.; Pavanello, M.; Zhou, J.; Kuai, X.; Gao, L.; He, H.; Wang, Y. Structural Transformation of Li-Excess Cathode Materials via Facile Preparation and Assembly of Sonication-Induced Colloidal Nanocrystals for Enhanced Lithium Storage Performance. *ACS Appl. Mater. Interfaces* **2017**, *9* (36), 31181–31191. https://doi.org/10.1021/acsami.7b09981.

(18) Xie, Y.; Chen, S.; Yang, W.; Zou, H.; Lin, Z.; zhou, J. Improving the Rate Capability and Decelerating the Voltage Decay of Li-Rich Layered Oxide Cathodes by Constructing a Surface-Modified Microrod Structure. *J. Alloys Compd.* **2019**, *772*, 230–239. https://doi.org/10.1016/j.jallcom.2018.09.046.

(19) Yang, Z.; Zhong, J.; Liu, Y.; Li, Z.; Li, J.; Yang, K. Unveiling the Effect of Voltage Regulation System on the Structure and Electrochemical Properties of Lithium-Rich Cathode Materials. *J. Electrochem. Soc.* **2019**, *166* (8), A1481–A1489.

https://doi.org/10.1149/2.0371908jes.

(20) Zhang, S.; Tang, T.; Ma, Z.; Gu, H.; Du, W.; Gao, M.; Liu, Y.; Jian, D.; Pan, H. Tuning Li2MO3 Phase Abundance and Suppressing Migration of Transition Metal Ions to Improve the Overall Performance of Li- and Mn-Rich Layered Oxide Cathode. *J. Power Sources* **2018**, *380* (January), 1–11. https://doi.org/10.1016/j.jpowsour.2018.01.045.

(21) Mori, D.; Sakaebe, H.; Shikano, M.; Kojitani, H.; Tatsumi, K.; Inaguma, Y. Synthesis, Phase Relation and Electrical and Electrochemical Properties of Ruthenium-Substituted Li_2MnO_3 as a Novel Cathode Material. *J. Power Sources* **2011**, *196* (16), 6934–6938. https://doi.org/10.1016/j.jpowsour.2010.11.150.

(22) Zou, T.; Qi, W. J.; Liu, X. S.; Wu, X. Q.; Fan, D. H.; Guo, S. H.; Wang, L. Improvement of the Electrochemical Performance of $Li_{1.2}Ni_{0.13}Co_{0.13}Mn_{0.54}O_2$ Cathode Material by Al_2O_3 Surface Coating. *J. Electroanal. Chem.* **2020**, *859*, 113845. https://doi.org/10.1016/j.jelechem.2020.113845.

(23) Zheng, J.; Gu, M.; Xiao, J.; Polzin, B. J.; Yan, P.; Chen, X.; Wang, C.; Zhang, J. G. Functioning Mechanism of AlF_3 Coating on the Li- and Mn-Rich Cathode Materials. *Chem. Mater.* **2014**, *26* (22), 6320–6327. https://doi.org/10.1021/cm502071h.

(24) Li, X.; Zhang, K.; Mitlin, D.; Yang, Z.; Wang, M.; Tang, Y.; Jiang, F.; Du, Y.; Zheng, J. Fundamental Insight into Zr Modification of Li- and Mn-Rich Cathodes: Combined Transmission Electron Microscopy and Electrochemical Impedance Spectroscopy Study. *Chem. Mater.* **2018**, *30* (8), 2566–2573. https://doi.org/10.1021/acs.chemmater.7b04861.

(25) Bao, L.; Yang, Z.; Chen, L.; Su, Y.; Lu, Y.; Li, W.; Yuan, F.; Dong, J.; Fang, Y.; Ji, Z.; Shi, C.; Feng, W. The Effects of Trace Yb Doping on the Electrochemical Performance of

Li-Rich Layered Oxides. *ChemSusChem* **2019**, *12* (10), 2294–2301. https://doi.org/10.1002/cssc.201900226.

(26) Chen, S.; Chen, Z.; Xia, M.; Cao, C.; Luo, Y. Toward Alleviating Voltage Decay by Sodium Substitution in Lithium-Rich Manganese-Based Oxide Cathodes. *ACS Appl. Energy Mater.* **2018**, *1* (8), 4065–4074. https://doi.org/10.1021/acsaem.8b00740.

(27) Ding, X.; Li, Y. X.; Wang, S.; Dong, J. M.; Yasmin, A.; Hu, Q.; Wen, Z. Y.; Chen, C. H. Towards Improved Structural Stability and Electrochemical Properties of a Li-Rich Material by a Strategy of Double Gradient Surface Modification. *Nano Energy* **2019**, *61*, 411–419. https://doi.org/10.1016/j.nanoen.2019.04.078.

(28) Liu, Y.; Wang, J.; Wu, J.; Ding, Z.; Yao, P.; Zhang, S.; Chen, Y. 3D Cube-Maze-Like Li-Rich Layered Cathodes Assembled from 2D Porous Nanosheets for Enhanced Cycle Stability and Rate Capability of Lithium-Ion Batteries. *Adv. Energy Mater.* **2020**, *10* (5), 1–10. https://doi.org/10.1002/aenm.201903139.

(29) Zhang, Y.; Zhang, W.; Shen, S.; Yan, X.; Wu, A.; Wu, R.; Zhang, J. An Ingenious Design of Lamellar $Li_{1.2}Mn_{0.54}Ni_{0.13}Co_{0.13}O_2$ Hollow Nanosphere Cathode for Advanced Lithium-Ion Batteries. *Electrochim. Acta* **2017**, *256*, 316–324. https://doi.org/10.1016/j.electacta.2017.09.150.

(30) Cui, B.; Zhang, J.; Liu, S.; Liu, X.; Xiang, W.; Liu, L.; Xin, H.; Lefler, M. J.; Licht, S. Electrochemical Synthesis of Ammonia Directly from N2 and Water over Iron-Based Catalysts Supported on Activated Carbon. *Green Chem.* **2017**, *19* (1), 298–304. https://doi.org/10.1039/c6gc02386j.

(31) Yan, W.; Xie, Y.; Jiang, J.; Sun, D.; Ma, X.; Lan, Z.; Jin, Y. Enhanced Rate Performance

of Al-Doped Li-Rich Layered Cathode Material via Nucleation and Post-Solvothermal Method. *ACS Sustain. Chem. Eng.* **2018**, *6* (4), 4625–4632. https://doi.org/10.1021/acssuschemeng.7b03634.

(32) Liu, D.; Fan, X.; Li, Z.; Liu, T.; Sun, M.; Qian, C.; Ling, M.; Liu, Y.; Liang, C. A Cation/Anion Co-Doped $Li_{1.12}Na_{0.08}Ni_{0.2}Mn_{0.6}O_{1.95}F_{0.05}$ Cathode for Lithium Ion Batteries. *Nano Energy* **2019**, *58*, 786–796. https://doi.org/10.1016/j.nanoen.2019.01.080.

(33) Laisa, C. P.; Ramesha, R. N.; Ramesha, K. Enhanced Electrochemical Performance of Lithium Rich Layered Cathode Materials by Ca2+ Substitution. *Electrochim. Acta* **2017**, *256*, 10–18. https://doi.org/10.1016/j.electacta.2017.10.029.

(34) Xie, Q.; Li, W.; Manthiram, A. A Mg-Doped High-Nickel Layered Oxide Cathode Enabling Safer, High-Energy-Density Li-Ion Batteries. *Chem. Mater.* **2019**, *31* (3), 938–946. https://doi.org/10.1021/acs.chemmater.8b03900.

(35) Nayak, P. K.; Grinblat, J.; Levi, E.; Levi, M.; Markovsky, B.; Aurbach, D. Understanding the Influence of Mg Doping for the Stabilization of Capacity and Higher Discharge Voltage of Li- and Mn-Rich Cathodes for Li-Ion Batteries. *Phys. Chem. Chem. Phys.* **2017**, *19* (8), 6142–6152. https://doi.org/10.1039/c6cp07383b.

(36) Vivekanantha, M.; Senthil, C.; Kesavan, T.; Partheeban, T.; Navaneethan, M.; Senthilkumar, B.; Barpanda, P.; Sasidharan, M. Reactive Template Synthesis of $Li_{1.2}Mn_{0.54}Ni_{0.13}Co_{0.13}O_2$ Nanorod Cathode for Li-Ion Batteries: Influence of Temperature over Structural and Electrochemical Properties. *Electrochim. Acta* **2019**, *317*, 398–407. https://doi.org/10.1016/j.electacta.2019.05.095.

(37) Prakasha, K. R.; Sathish, M.; Bera, P.; Prakash, A. S. Mitigating the Surface Degradation

and Voltage Decay of $Li_{1.2}Ni_{0.13}Mn_{0.54}Co_{0.13}O_2$ Cathode Material through Surface Modification Using Li_2ZrO_3. *ACS Omega* **2017**, *2* (5), 2308–2316. https://doi.org/10.1021/acsomega.7b00381.

(38) Zhang, X.; Jiang, W. J.; Mauger, A.; Qilu; Gendron, F.; Julien, C. M. Minimization of the Cation Mixing in $Li_{1+x}(NMC)_{1-X}O_2$ as Cathode Material. *J. Power Sources* **2010**, *195* (5), 1292–1301. https://doi.org/10.1016/j.jpowsour.2009.09.029.

(39) Remith, P.; Kalaiselvi, N. $Li_{1.2}Mn_{0.6}Ni_{0.1}Co_{0.1}O_2$ Microspheres Constructed by Hierarchically Arranged Nanoparticles as Lithium Battery Cathode with Enhanced Electrochemical Performance. *Nanoscale* **2014**, *6* (24), 14724–14732. https://doi.org/10.1039/c4nr04314f.

(40) Luo, K.; Roberts, M. R.; Hao, R.; Guerrini, N.; Pickup, D. M.; Liu, Y. S.; Edström, K.; Guo, J.; Chadwick, A. V.; Duda, L. C.; Bruce, P. G. Charge-Compensation in 3d-Transition-Metal-Oxide Intercalation Cathodes through the Generation of Localized Electron Holes on Oxygen. *Nat. Chem.* **2016**, *8* (7), 684–691. https://doi.org/10.1038/nchem.2471.

(41) Saroha, R.; Cho, J. S.; Ahn, J. H. Synergetic Effects of Cation (K+) and Anion (S2−)-Doping on the Structural Integrity of Li/Mn-Rich Layered Cathode Material with Considerable Cyclability and High-Rate Capability for Li-Ion Batteries. *Electrochim. Acta* **2021**, *366*, 137471. https://doi.org/10.1016/j.electacta.2020.137471.

(42) Yi, L.; Liu, Z.; Yu, R.; Zhao, C.; Peng, H.; Liu, M.; Wu, B.; Chen, M.; Wang, X. Li-Rich Layered/Spinel Heterostructured Special Morphology Cathode Material with High Rate Capability for Li-Ion Batteries. *ACS Sustain. Chem. Eng.* **2017**, *5* (11), 11005–11015.

https://doi.org/10.1021/acssuschemeng.7b02906.

(43) He, W.; Yuan, D.; Qian, J.; Ai, X.; Yang, H.; Cao, Y. Enhanced High-Rate Capability and Cycling Stability of Na-Stabilized Layered $Li_{1.2}[Co_{0.13}Ni_{0.13}Mn_{0.54}]O_2$ Cathode Material. *J. Mater. Chem. A* **2013**, *1* (37), 11397–11403. https://doi.org/10.1039/c3ta12296d.

(44) Debasish, M.; Jianlin, L., Daniel, P., A.; Ashfia, H.; Andrew, P.; David, L., W.; Claus, D. Unraveling the Voltage-Fade Mechanism in High-Energy-Density Lithium-Ion Batteries: Origin of the Tetrahedral Cations for Spinel Conversion. *Chem. Mater*. **2014**, 26 (21), 6272-6280, https://doi.org/10.1021/cm5031415.

(45) Chen, S.; Xie, Y.; Chen, W.; Chen, J.; Yang, W.; Zou, H.; Lin, Z. Enhanced Electrochemical Performance of Li-Rich Cathode Materials by Organic Fluorine Doping and Spinel $Li_{1+X}Ni_yMn_{2-Y}O_4$ Coating. *ACS Sustain. Chem. Eng.* **2020**, *8* (1), 121–128. https://doi.org/10.1021/acssuschemeng.9b04665.

(46) Lee, E. S.; Huq, A.; Chang, H. Y.; Manthiram, A. High-Voltage, High-Energy Layered-Spinel Composite Cathodes with Superior Cycle Life for Lithium-Ion Batteries. *Chem. Mater*. **2012**, *24* (3), 600–612. https://doi.org/10.1021/cm2034992.

(47) Duraisamy, S.; Penki, T. R.; Kishore, B.; Barpanda, P.; Nayak, P. K.; Aurbach, D.; Munichandraiah, N. Porous, Hollow $Li_{1.2}Mn_{0.53}Ni_{0.13}Co_{0.13}O_2$ Microspheres as a Positive Electrode Material for Li-Ion Batteries. *J. Solid State Electrochem.* **2017**, *21* (2), 437–445. https://doi.org/10.1007/s10008-016-3380-7.

(48) Kesavan, T.; Senthil, C.; Sasidharan, M. Solvothermally Synthesized Ti-Rich $LiMnTiO_4$ as Cathode Material for High Li Storage. *J. Mater. Sci.* **2018**, *53* (6), 4406–4416. https://doi.org/10.1007/s10853-017-1819-6.

(49) Nguyen, V. H.; Shim, J. J. In Situ Growth of Hierarchical Mesoporous $NiCo_2S_4$@MnO_2 Arrays on Nickel Foam for High-Performance Supercapacitors. *Electrochim. Acta* **2015**, *166*, 302–309. https://doi.org/10.1016/j.electacta.2015.03.069.

(50) Ma, D.; Li, Y.; Wu, M.; Deng, L.; Ren, X.; Zhang, P. Enhanced Cycling Stability of Li-Rich Nanotube Cathodes by 3D Graphene Hierarchical Architectures for Li-Ion Batteries. *Acta Mater.* **2016**, *112*, 11–19. https://doi.org/10.1016/j.actamat.2016.04.010.

(51) Chen, Z.; Wang, J.; Chao, D.; Baikie, T.; Bai, L.; Chen, S.; Zhao, Y.; Sum, T. C.; Lin, J.; Shen, Z. Hierarchical Porous $LiNi_{1/3}Co_{1/3}Mn_{1/3}O_2$ Nano-/Micro Spherical Cathode Material: Minimized Cation Mixing and Improved Li + Mobility for Enhanced Electrochemical Performance. *Sci. Rep.* **2016**, *6* (February), 1–10. https://doi.org/10.1038/srep25771.

(52) Wu, L. Q.; Li, Y. C.; Li, S. Q.; Li, Z. Z.; Tang, G. D.; Qi, W. H.; Xue, L. C.; Ge, X. S.; Ding, L. L. Method for Estimating Ionicities of Oxides Using O1s Photoelectron Spectra. *AIP Adv.* **2015**, *5* (9). https://doi.org/10.1063/1.4931996.

(53) Rodrigues, A.; Bauer, S.; Baumbach, T. Effect of Post-Annealing on the Chemical State and Crystalline Structure of PLD $Ba_{0.5}Sr_{0.5}TiO_3$ Films Analyzed by Combined Synchrotron X-Ray Diffraction and X-Ray Photoelectron Spectroscopy. *Ceram. Int.* **2018**, *44* (13), 16017–16024. https://doi.org/10.1016/j.ceramint.2018.06.038.

(54) Greczynski, G.; Hultman, L. X-Ray Photoelectron Spectroscopy: Towards Reliable Binding Energy Referencing. *Prog. Mater. Sci.* **2020**, *107* (April 2019), 100591. https://doi.org/10.1016/j.pmatsci.2019.100591.

(55) Vivekanantha, M.; Partheeban, T.; Kesavan, T.; Senthil, C.; Sasidharan, M. Alleviating

the Initial Coulombic Efficiency Loss and Enhancing the Electrochemical Performance of $Li_{1.2}Mn_{0.54}Ni_{0.13}Co_{0.13}O_2$ Using β-MnO_2. *Appl. Surf. Sci.* **2019**, *489* (May), 336–345. https://doi.org/10.1016/j.apsusc.2019.05.342.

(56) Assat, G.; Foix, D.; Delacourt, C.; Iadecola, A.; Dedryvère, R.; Tarascon, J. M. Fundamental Interplay between Anionic/Cationic Redox Governing the Kinetics and Thermodynamics of Lithium-Rich Cathodes. *Nat. Commun.* **2017**, *8* (1). https://doi.org/10.1038/s41467-017-02291-9.

Figure Captions

Scheme 1. Schematic Representation of PLR and SLR cathodes

Table 1. Refined lattice and Rietveld parameters for XRD Diffractograms

Fig. 1 XRD patterns of PLR, SLR-0.0015, SLR-0.003, SLR-0.005 and SLR- 0.007

Fig. 2 **a-e.** Cyclic voltametry plots of: (a) PLR; (b) SLR-0.0015; (c) SLR-0.003; (d) SLR-0.005; (e) SLR-0.007, and (f) 5^{th} cycle comparison plots at a scan rate of 0.2 mV/s in the voltage window of 2.0-4.8 V (*vs*. Li/Li^+)

Fig. 3 (a) 1st cycle GCPL plots of PLR and SLR series; (b) Cycle life performance of PLR and SLR; (c) Energy density plot of PLR and SLR series; (d-e) Comparative GCPL plots of PLR and SLR-0.005; (e) Average voltage plot of PLR and SLR series; (f) Rate capability plot of PLR and SLR series

Fig. 4 (a-c) SEM images of SLR-0.005; (d-i) Elemental mapping of SLR -0.005; (j-k) TEM images of SLR-0.005; (l) HR-TEM images of SLR-0.005; and (m) SAED pattern for SLR-0.005

Fig. 5 (a-b) Rietveld patterns of PLR and SLR-0.005; (c-d) Comparison of fresh and cycled XRD patterns of PLR and SLR-0.005 after 1^{st} charge and 1^{st} discharge; (e-f) XRD patterns of PLR and SLR-0.005 before and after cycling (125 cycles) at 0.5 C

Fig. 6 Deconvoluted XPS spectra of SLR-0.005: (a) Mn 2p; (b) Co 2p; (c) Ni 2p; (d) Sr 3d; (e) O 1s; (f) Survey spectra for SLR-0.005; and (g-j) XPS stacking plots of

PLR and SLR-0.005

Fig. 7 (a) Comparative 1st cycle dQ/dV plots of PLR and SLR-0.005; (b) Comparative dQ/dV plots of PLR and SLR-0.005 after 125 cycles at 0.5 C (c-d) dQ/dV plots of different cycles for PLR and SLR-0.005 at 0.5 C respectively.

Fig. 8 (a) Cycle life performance of PLR and SLR -0.005 at 1C; (b) Energy density plot of PLR and SLR-0.005 at 1C; (c) Average voltage plot of PLR and SLR-0.005 at 1C; and (d, e) Average charge and discharge voltage plots for PLR and SLR-0.005.

Fig. 9 (a) (a) Cycle life performance of PLR and SLR -0.005 at 55 °C; (b) Energy density plot of PLR and SLR-0.005 at 55 °C; (c) Average voltage plot of PLR and SLR-0.005 at 55 °C; (d) 1st cycle dQ/dV plots of PLR and SLR-0.005 at 55 °C; and (e,f) dQ/dV plots of PLR and SLR-0.005 at 55 °C.

Fig. 10 (a) 1st GCPL plots of PLR and SLR-0.005 full cell; (b) Cycle life performance of PLR and SLR-0.005 full cells (inset) SLR-0.005 up to 100 cycles; (c & d) GCPL profiles of PLR and SLR-0.005.

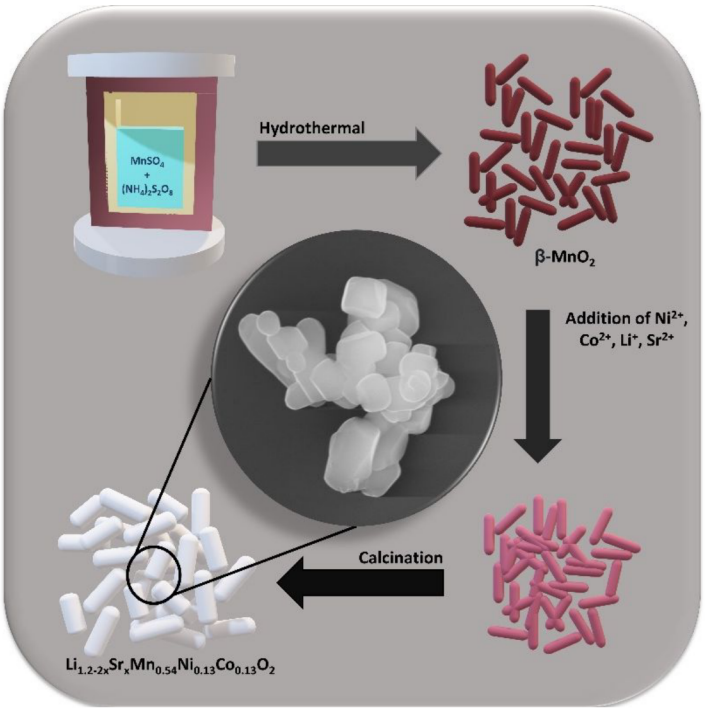

Scheme 1. Schematic representation of synthesis of PLR and SLR cathodes.

Table 1. Refined lattice and Rietveld parameters for XRD Diffractograms

Sample	*a* (Å)	*b* (Å)	*c* (Å)	*β*	Volume (Å^3)	R_{wp} (%)
PLR	4.9536(3)	8.5516(2)	5.0318(5)	109.2(2)	200.2(4)	7.8
SLR-0.005	4.9440(4)	8.5511(2)	5.0460(3)	109.2(1)	200.5(2)	5.7

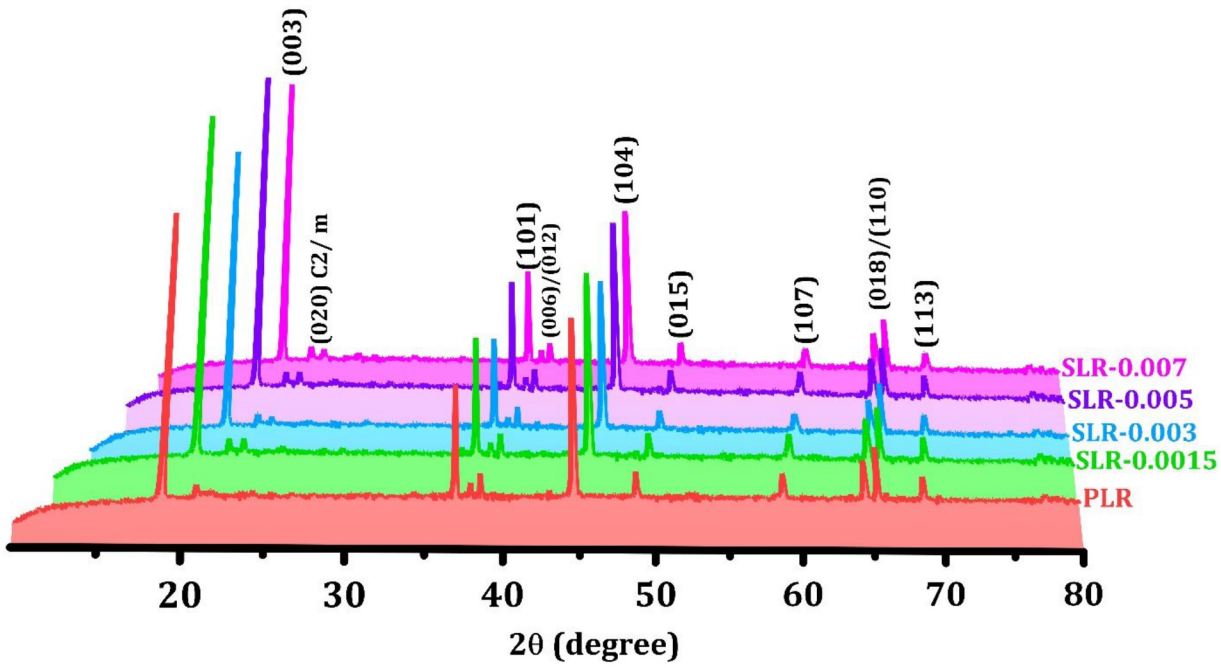

Fig. 1. XRD patterns of PLR, SLR-0.0015, SLR-0.003, SLR-0.005, and SLR- 0.007

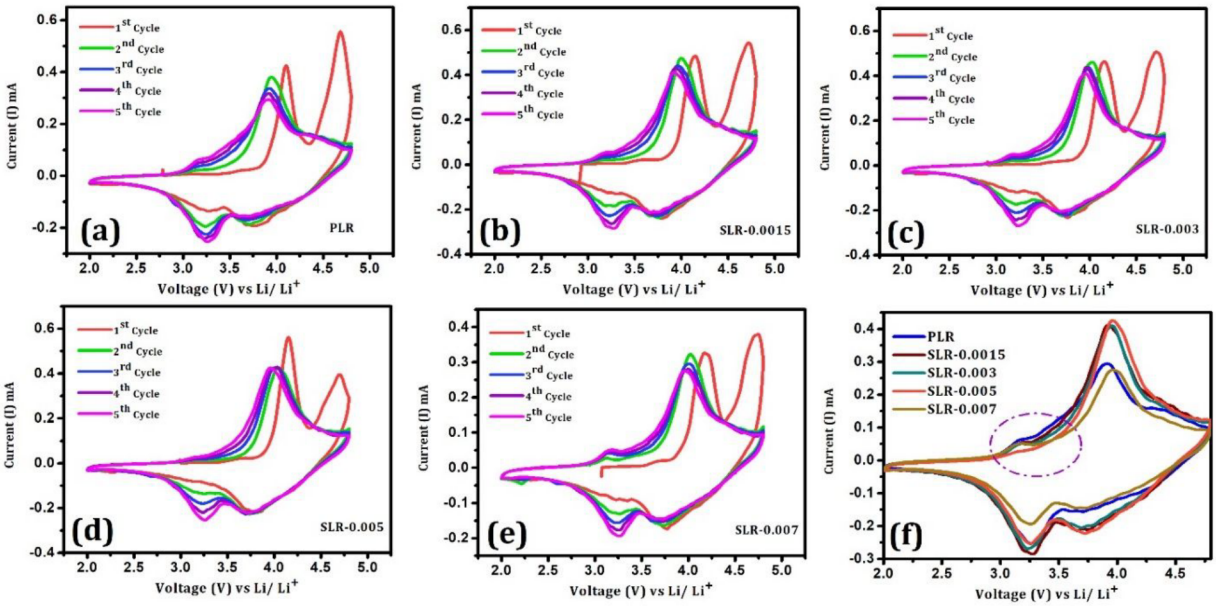

Fig. 2a-e. Cyclic voltametry plots of: (a) PLR; (b) SLR-0.0015; (c) SLR-0.003; (d) SLR-0.005; (e) SLR-0.007, and (f) 5th cycle comparison plots at a scan rate of 0.2 mV/s in the voltage window of 2.0-4.8 V (*vs*. Li/Li^{+})

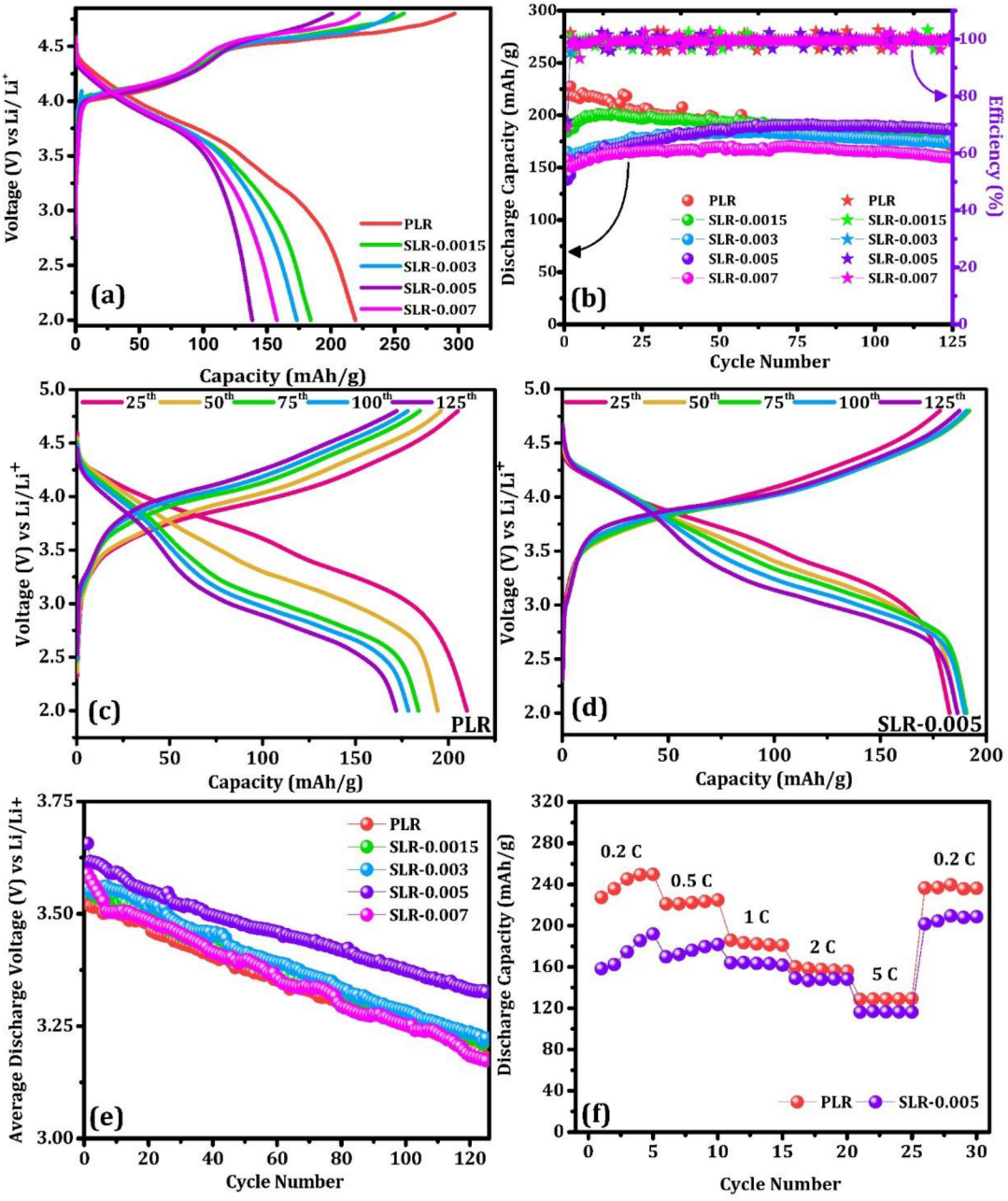

Fig. 3. (a) 1st cycle GCPL plots of PLR and SLR series; (b) Cycle life performance of PLR and SLR; (c) Energy density plot of PLR and SLR series; (d-e) Comparative GCPL plots of PLR and SLR-0.005; (e) Average voltage plot of PLR and SLR series; (f) Rate capability plot of PLR and SLR series

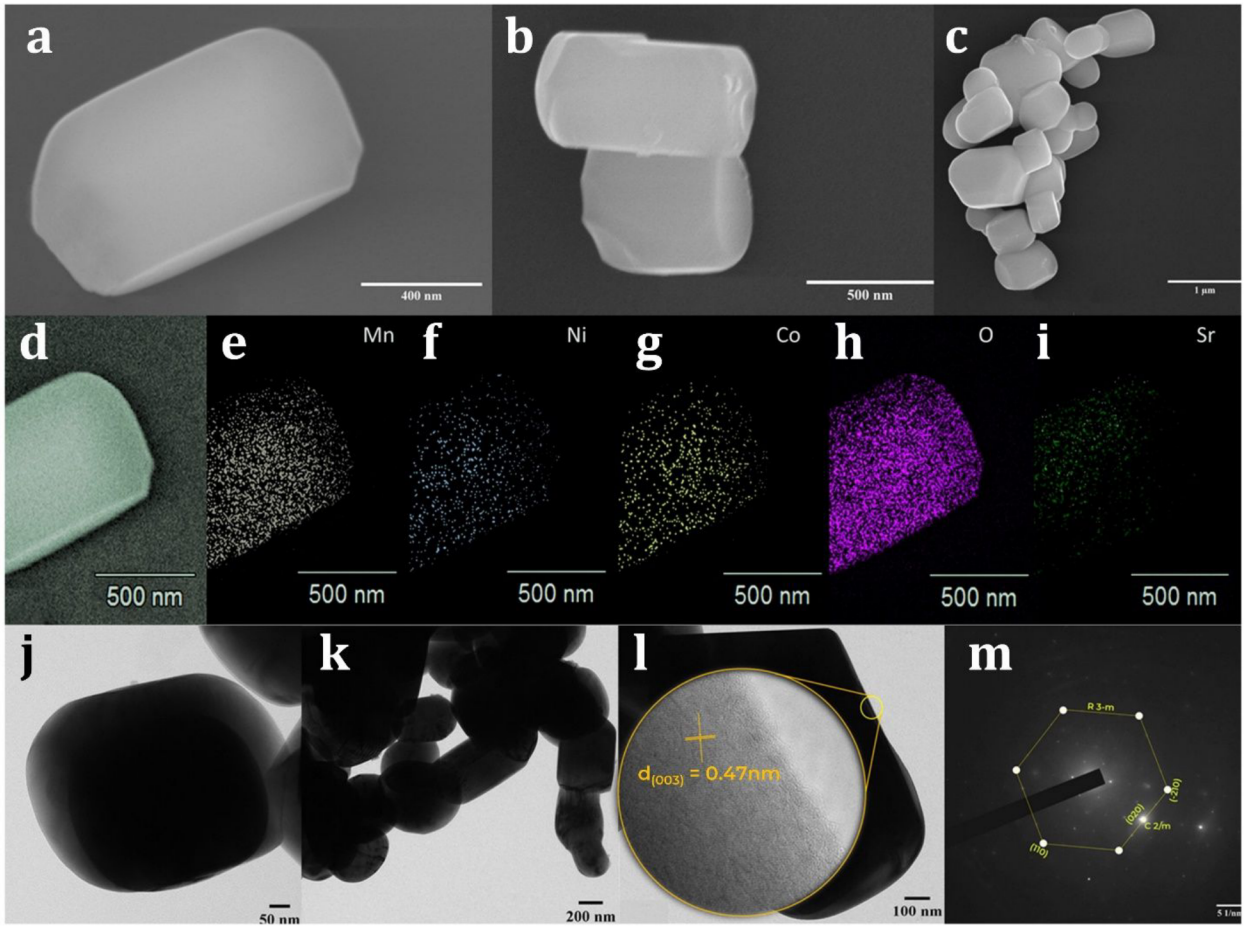

Fig. 4. (a-c) SEM images of SLR-0.005; (d-i) Elemental mapping of SLR -0.005; (j-k) TEM images of SLR-0.005; (l) HR-TEM images of SLR-0.005; and (m) SAED pattern for SLR-0.005

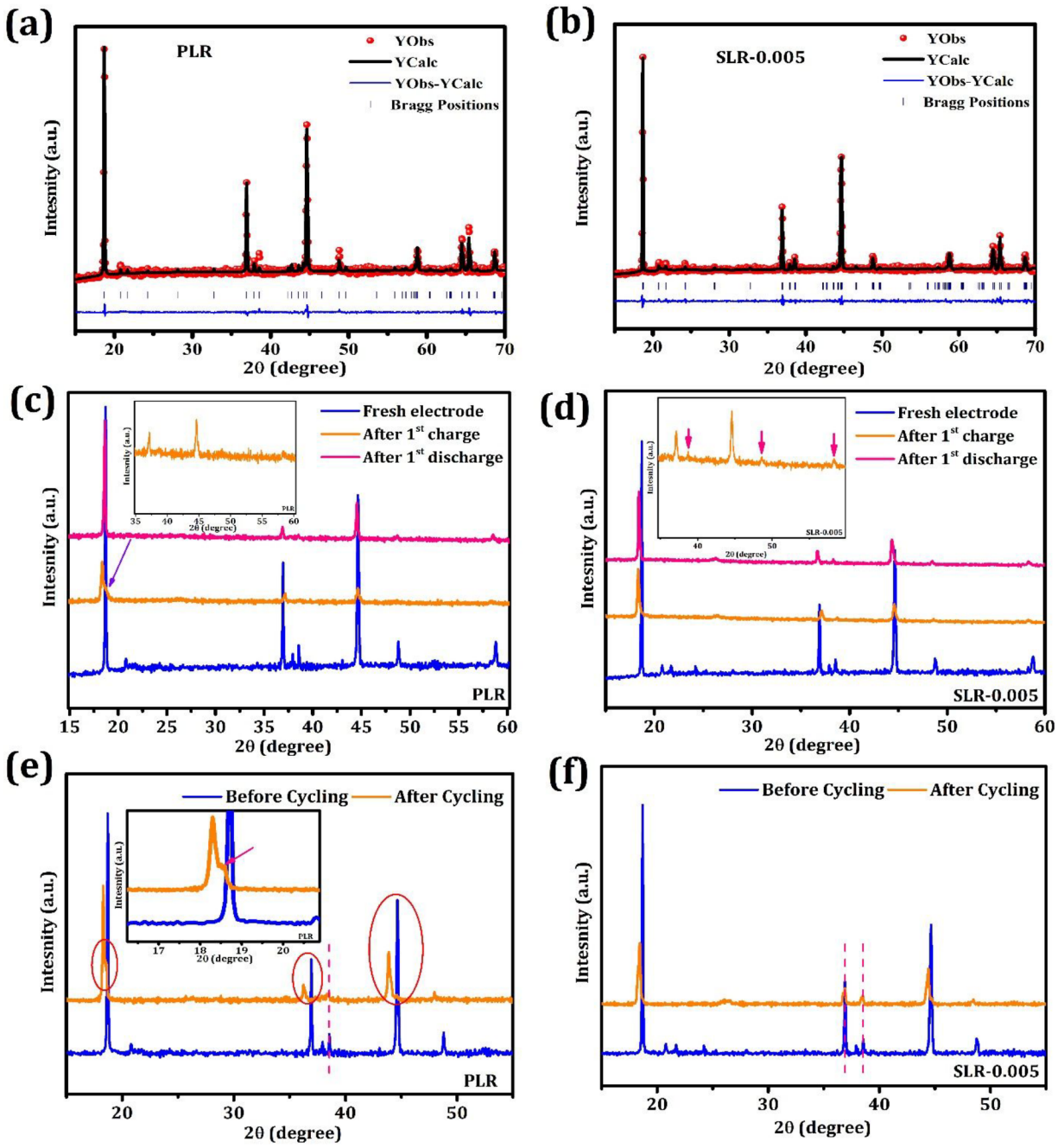

Fig. 5. (a-b) Rietveld patterns of PLR and SLR-0.005; (c-d) Comparison of fresh and cycled XRD patterns of PLR and SLR-0.005 after 1st charge and 1st discharge; (e-f) XRD patterns of PLR and SLR-0.005 before and after cycling (125 cycles) at 0.5 C

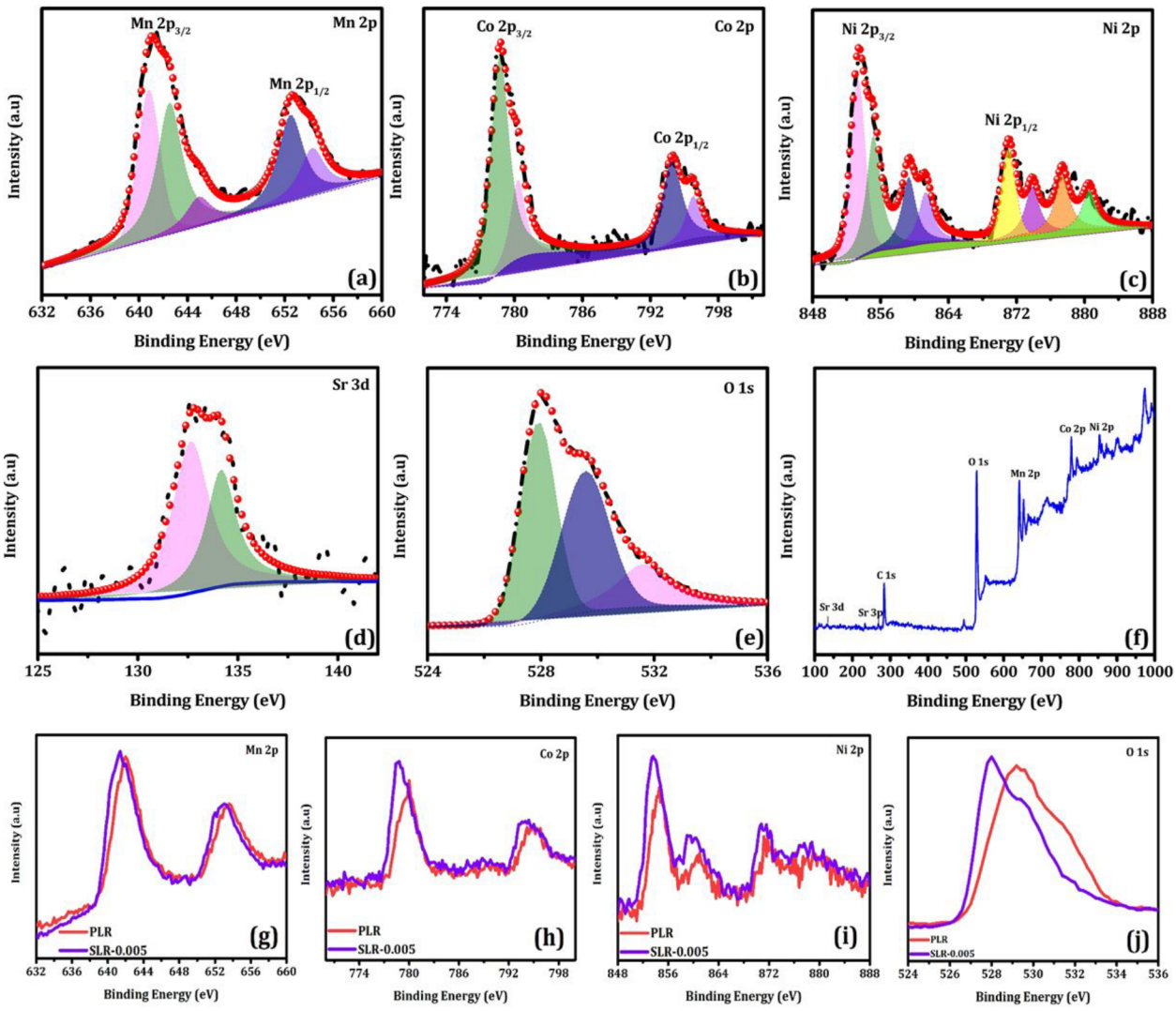

Fig. 6. Deconvoluted XPS spectra of SLR-0.005: (a) Mn 2p; (b) Co 2p; (c) Ni 2p; (d) Sr 3d; (e) O 1s; (f) Survey spectra for SLR-0.005; and (g-j) XPS stacking plots of PLR and SLR-0.005

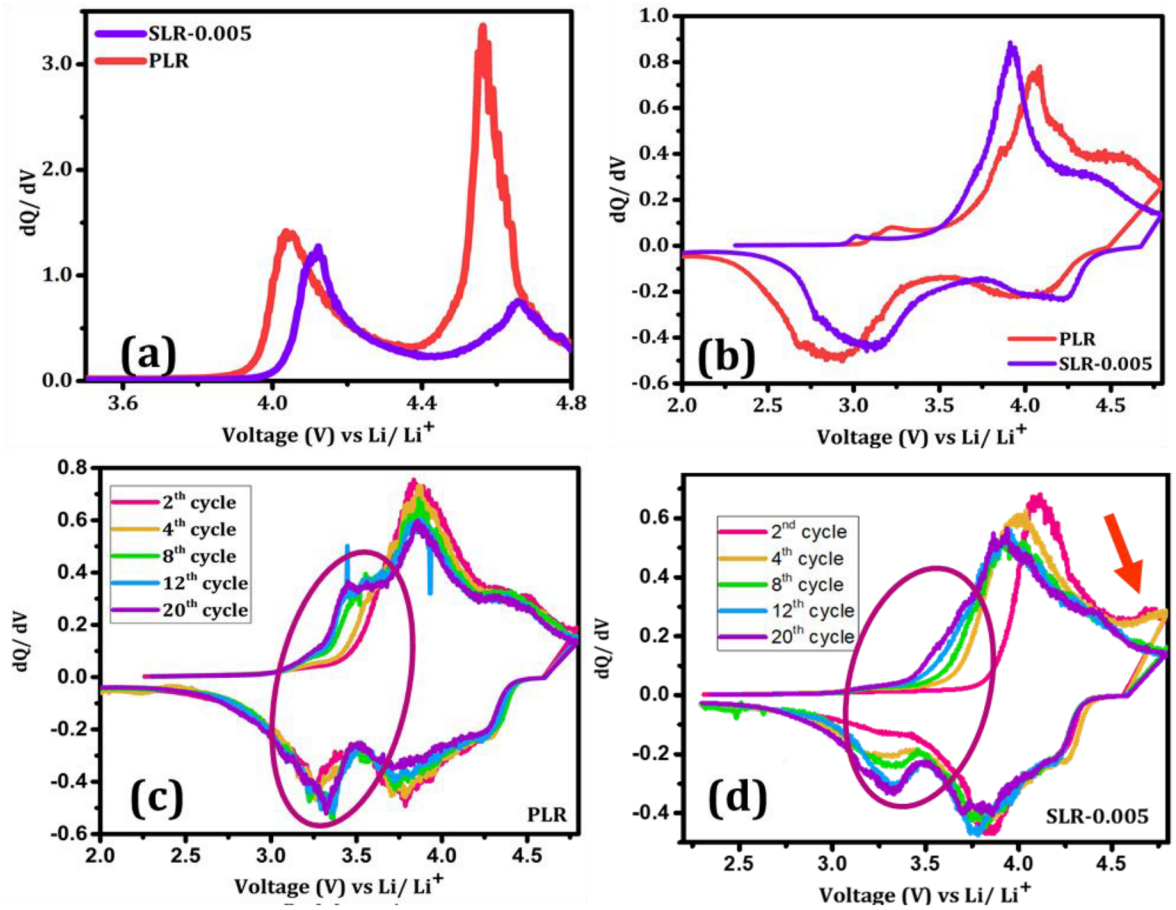

Fig. 7. (a) Comparative 1st cycle dQ/dV plots of PLR and SLR-0.005; (b) Comparative dQ/dV plots of PLR and SLR-0.005 after 125 cycles at 0.5 C (c-d) dQ/dV plots of different cycles for PLR and SLR-0.005 at 0.5 C respectively.

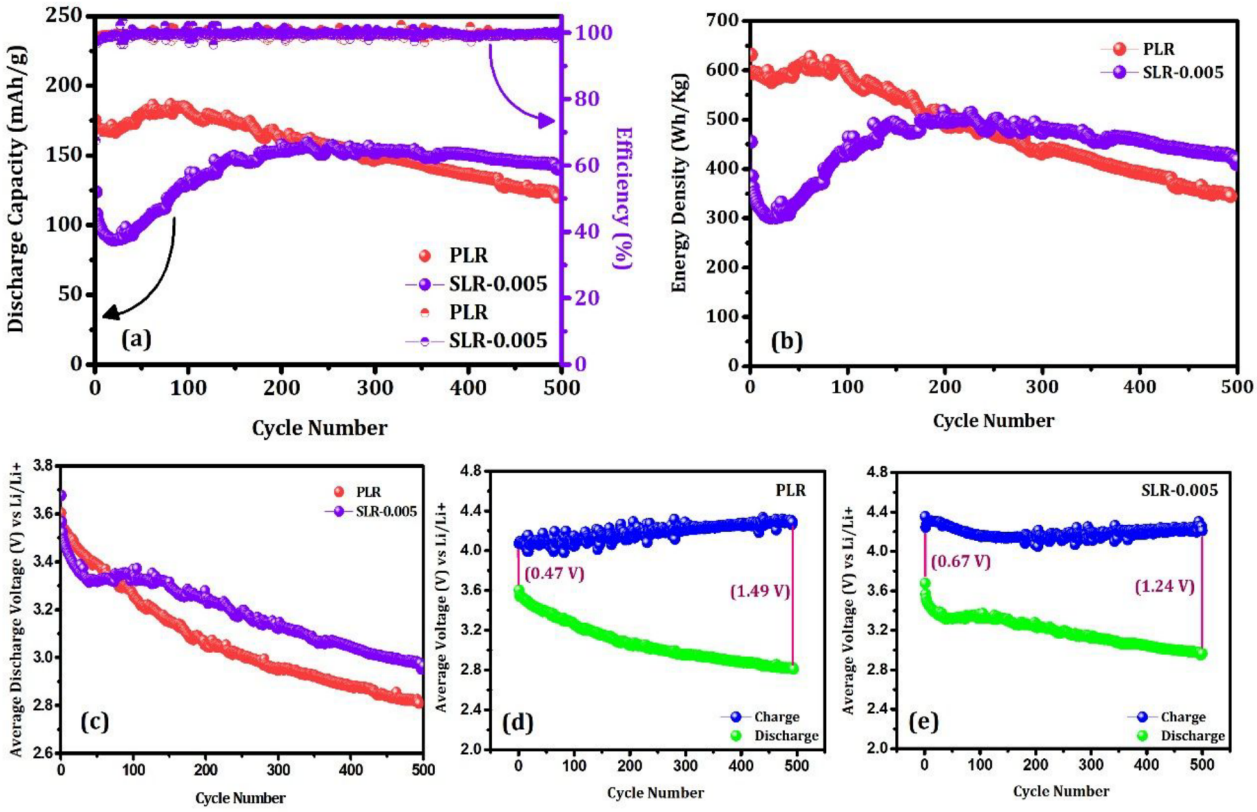

Fig. 8. (a) Cycle life performance of PLR and SLR -0.005 at 1 C; (b) Energy density plot of PLR and SLR-0.005 at 1 C; (c) Average voltage plot of PLR and SLR-0.005 at 1 C; and (d, e) Average charge and discharge voltage plots for PLR and SLR-0.005.

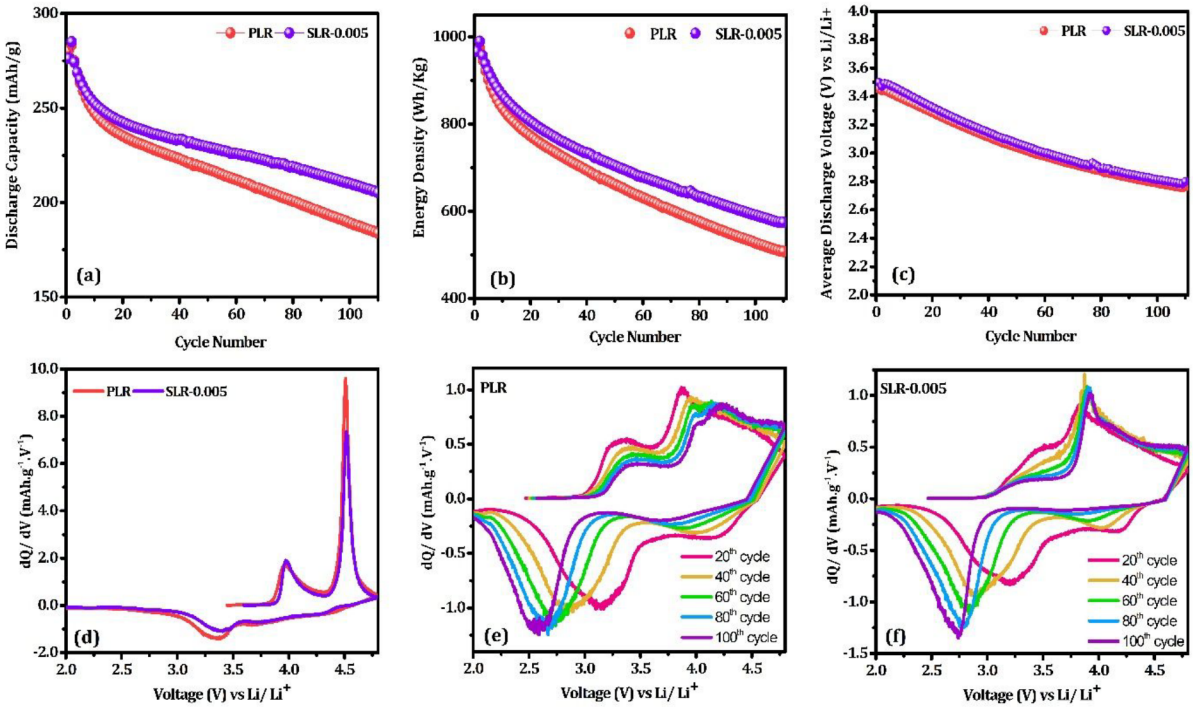

Fig. 9. (a) Cycle life performance of PLR and SLR -0.005 at 55 °C; (b) Energy density plot of PLR and SLR-0.005 at 55 °C; (c) Average voltage plot of PLR and SLR-0.005 at 55 °C; (d) 1st cycle dQ/dV plots of PLR and SLR-0.005 at 55 °C; and (e,f) dQ/dV plots of PLR and SLR-0.005 at 55 °C.

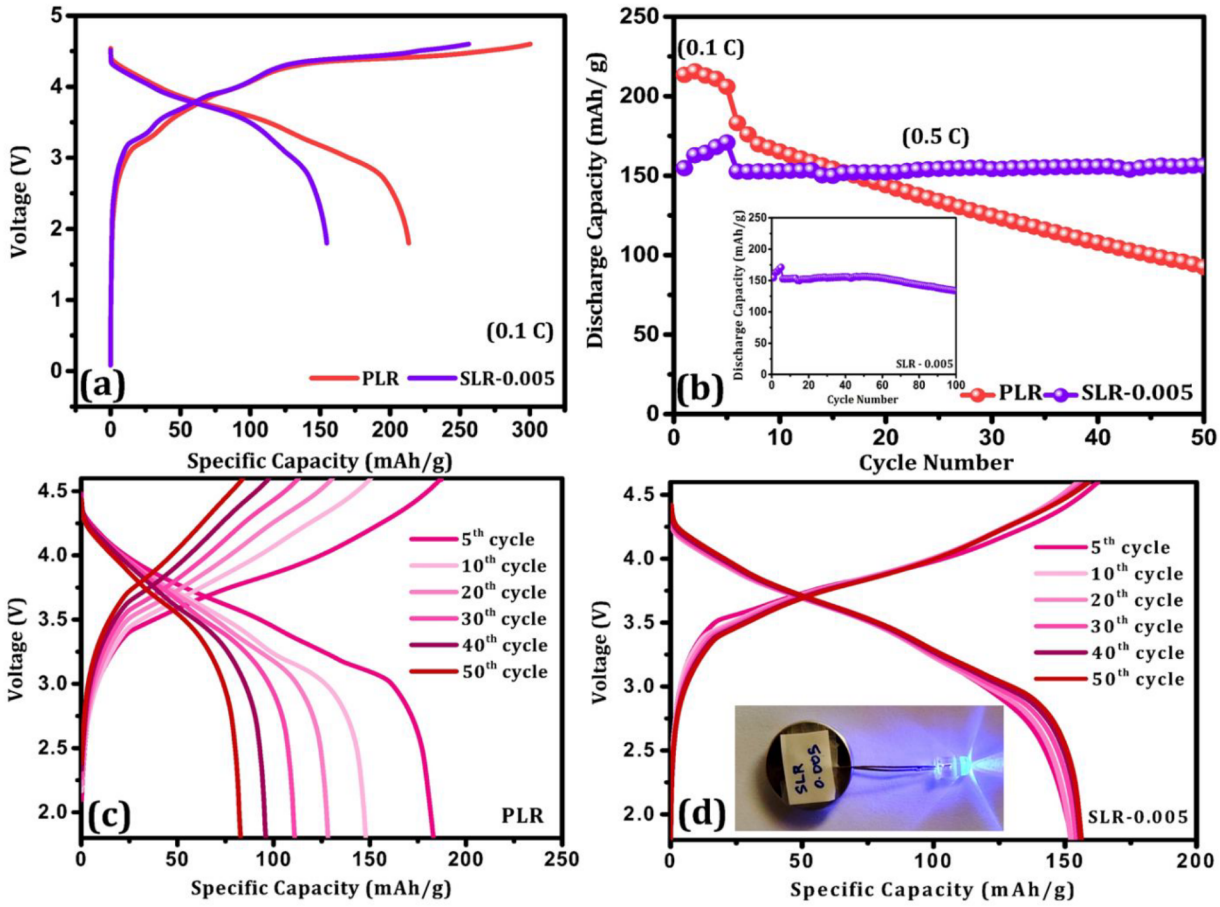

Fig. 10. (a) 1st GCPL plots of PLR and SLR-0.005 full cell; (b) Cycle life performance of PLR and SLR-0.005 full cells (inset) SLR-0.005 up to 100 cycles; (c & d) GCPL profiles of PLR and SLR-0.005.

For Table of Contents Use Only

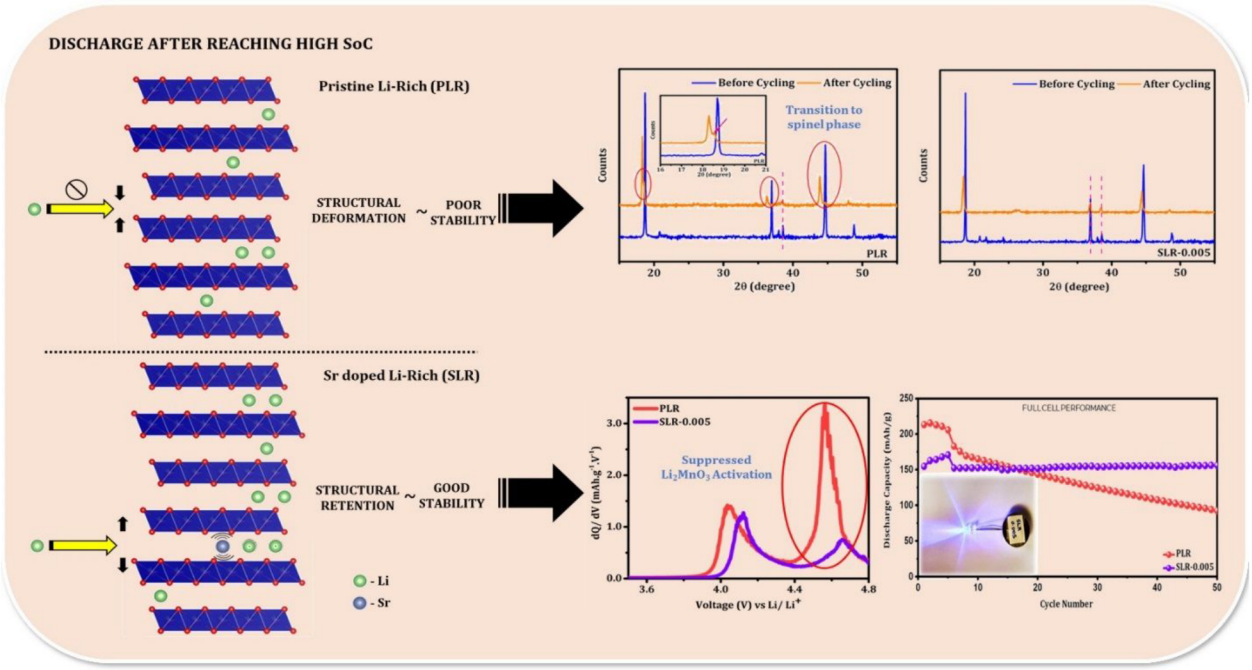

Synopsis

Strontium doping in $Li_{1.2}Mn_{0.54}Co_{0.13}Ni_{0.13}O_2$ results in suppression of anion-redox activity leading to a sustainable performance in real time practical applications.